Synthesis, characterization, and thermodynamic study of selected K-based zeolites

Bin Ma [a],[*], Barbara Lothenbach [a],[b]

[a] Laboratory for Concrete & Asphalt, Swiss Federal Laboratories for Materials Science and Technology (Empa), 8600 Dübendorf, Switzerland
[b] Department of Structural Engineering, Norwegian University of Science and Technology (NTNU), 7491 Trondheim, Norway

ARTICLE INFO

ABSTRACT

Potassium-rich zeolites often occur in cementitious systems, as K^+ is widespread in various cementitious materials, such as Portland, blended and alkali-activated cements. The knowledge of their stability and of thermodynamic models for solid solutions with Na^+ and Ca^{2+} are critical to understand long-term development and durability in such cements. Completing previous studies on Na- and Ca-based zeolites, the current work aims to determine the thermodynamic data of 14 types of K-based zeolites, which could possibly form in cementitious systems. The zeolites were synthesized hydrothermally, exchanged with K^+, and characterized thoroughly with respect to framework structures, elemental compositions, water contents, and bond variations. Their thermodynamic properties were derived from the experimental solubility data, which allowed establishing predominance diagrams in the K_2O-SiO_2-Al_2O_3-H_2O system. The K-based zeolites typically showed the lowest solubility between 0 and 100 °C, with the notable exception of Ca-gismondine and two Na-based zeolites: natrolite and Na-mordenite.

1. Introduction

Zeolites are expected to exist universally in and/or at the surface of cementitious systems. Zeolites are used as supplementary cementitious materials aiming at a reduction of CO_2 emission [1], they can also be formed in alkali-activated cements [2–4], in ancient Roman cements [5], in Al-rich chemical environments relevant to alkali silica reaction (ASR) [6,7], and in the long-term interaction zones of degraded hydrated Portland cements and clays or rock-forming minerals [8–12]. Such interaction zones are widespread in underground concrete structures, such as tunnels, sluices, cementitious nuclear waste repositories, dams and more, which are in close contact with the surrounding minerals.

Although zeolites occur in various environments, limited thermodynamic data based on experimental solubility measurements for zeolites are available, which largely limits a reliable prediction of the stability domains (i.e., formation vs. dissolution) of zeolites. Zeolites, having microporous frameworks, are built primarily with AlO_4 and SiO_4 tetrahedra and incorporate charge-balancing cations in so-called cages. They have a general formula as $[M^{n+}]^+_{1/n}[AlSi_xO_{2x+2}]^- \cdot yH_2O$, where x $\geq$ 1 and M^{n+} represents the extra-framework cation (e.g., Na^+, K^+, and

Ca^{2+}) present in cages. The lack of reliable thermodynamic data is partially caused by the variable and often difficult to determine Al/Si ratios and the presence of different extra-framework cations of zeolites [8,13,14]. Thus, experienced researchers developed various theoretical estimation methods, such as the polymer model [14,15], additivity methods [16–18], exchange models [19], polyhedral model [20], and phase relation methods [18], to calculate the standard Gibbs free energy of formation (ΔG_f^0), the standard enthalpy of formation (ΔH_f^0), the standard entropy (S^0), and the standard heat capacity (C_p^0), based on elementary (hydro)oxide components. Although the calculation results have shown satisfactory consistency with the experimental data from calorimetry measurements [14,21,22], the solubility product (K_{sp}) derived from the estimated ΔH_f^0 and S^0 or from calorimetry data occasionally displayed considerable errors, which can result in unreasonable thermodynamic predictions [10]. In contrast, to measure the solubility of well-defined zeolites is a reliable method for determining the log K_{sp} values directly [23].

The thermodynamic properties based on experimental log K_{sp} values for selected Na- and Ca-based zeolites have been determined recently [10,24]. These thermodynamic data for zeolites, are fully compatible with the Cemdata18 database [25], as well as with the data for clays and

---

micas in THERMOCHIMIE database [26], as validated by establishing predominance diagrams. Only limited solubility data for K-based zeolite are available, although K$^+$ is a key cation often present in the zeolitic cages. For instance, K$^+$ is found to predominate the extra-framework cations in many natural zeolites, such as phillipsite, merlinoite, chabazite, clinoptilolite, and heulandite [27]. The naturally widespread existence of K-based zeolites indicates that K$^+$ may thermodynamically stabilize a certain zeolitic frameworks. K$^+$ also prevails in Portland cement, in blended [28] and in some alkali-activated cements [29,30]. Under the long-term interaction between cements and clays or rock forming minerals, K$^+$ seems to transfer into the secondary zeolites as the cage cation [12]. This very limited experimental evidence has been confirmed in several simulations of cement/clay interactions, in which K-rich phillipsite and chabazite were observed or predicted to form [11,31]. In contrast, the Na-endmember of phillipsite was not predicted in the predominance diagrams for Na$_2$O-SiO$_2$-Al$_2$O$_3$-H$_2$O sub-chemical systems [24], suggesting that the incorporation of K$^+$ into phillipsite could be favored thermodynamically over the incorporation of Na$^+$. To verify whether and to which extent K$^+$ stabilizes the zeolitic structure, the thermodynamic data of K-based zeolites need to be quantified accurately.

Typically, most zeolites, e.g., phillipsite, chabazite, and clinoptilolite, contain multiple types of extra-framework cations. In the presence of multiple cations (e.g., Na$^+$, K$^+$, Ca^{2+}, and Mg^{2+}), the most common case in actual environments, zeolites contain various cations, forming so-called solid solutions [32]. To establish the thermodynamic model for such zeolite solid solutions, fundamental data of all the different cation endmembers are required. This underlines the need for systematic experimental determination of the thermodynamic data for zeolite endmembers of different cations.

In this study, we aim to quantify the thermodynamic data of synthesized K-based zeolites that could be expected to form in cementitious systems and in nature by measuring their solubility products as a function of temperature. Predominance diagrams in K$_2$O-SiO$_2$-Al$_2$O$_3$-H$_2$O sub-chemical systems are established to verify the reliability of the currently generated zeolite data and their consistency with the available mainstream databases. The solubility-derived thermodynamic data support a reliable prediction of stability domains of K-based zeolites in not only the cement/clay or rock system but also any environment where K-based zeolites may exist.

2. Materials and methods

2.1. K-based zeolite synthesis

Fresh Milli-Q water (18.2 MΩ·cm) was used for all solutions and suspensions. All the K-based zeolites were obtained via hydrothermal cation exchange from the corresponding as-synthesized (i.e., ANA, LS-P (Na), PHI(NaK), LTA, CHA(Na), FAU-X, FAU-Y, NAT, and MOR(Na)) [24] or natural (i.e., STI, HEU_1, and CLI) [10] zeolites reported in our previous works. The detailed information of the zeolites used is shown in Table A1. Two additional types of Na-based zeolites, tetranatrolite (tetra-NAT) and gismondine-P1 (GIS-P1(Na)), were synthesized via hydrothermal methods, as detailed in a parallel study [33], and the cation exchanged as detailed above. Both tetranatrolite and natrolite belong to the family of NAT framework, whereas the former has a completely disordered distribution of Si and Al T-sites in tetragonal symmetry and can transform at long crystallization time into natrolite, which has ordered T-sites distribution in orthorhombic symmetry [34]. GIS-P1(Na) has the same framework of GIS but a higher Si/Al ratio compared with LS-P(Na) [35,36]. Typically, the hydrothermal cation exchange experiments were performed under an identical solid-to-liquid (S/L) ratio of 50 g L^{-1} using 3.0 M KNO$_3$ (99%, Sigma-Aldrich) solution. To achieve a nearly complete cation exchange, three exchange cycles were conducted. In each cycle, the suspension was equilibrated in a Teflon vessel at 80 °C for 24 h, followed by centrifuging to separate the

suspension and washing the remaining solid with Milli-Q water one time. Lastly, the solid product was collected by vacuum filtration, washed for four times to remove residual KNO$_3$, and dried in an oven at 80 °C. The dried zeolites were ground and sieved through a 63-μm mesh before being stored in a desiccator for further experiments. A constant 35% relative humidity and a low CO$_2$ level in the desiccator were controlled by saturated CaCl$_2$ solution and CO$_2$ trap, respectively.

2.2. Solid phase characterization

X-ray diffraction (XRD) analysis was employed to identify the secondary building unit (SBU) and the framework precisely, and the approximate chemical composition. A PANalytical X'Pert Pro diffractometer in horizontally oriented mounting mode was used to collect the XRD signal at a X-ray wavelength of 1.789 Å (Co Kα radiation) with a θ–2θ configuration. The chemical composition, except for the water content, of each zeolite was further determined by energy dispersive X-ray spectroscopy (EDS) analysis associated with scanning electron microscopy (SEM, Philips ESEM FEG XL 30) under a beam voltage of 15 keV. To improve the precision of EDS analysis, a relatively flat surface was prepared via pressing the powdered samples into pellets. Repeated measurements were conducted on three different flat areas (size: 50 μm × 50 μm) of each prepared pellet that was pasted on a carbon disc and then coated with carbon. An average was made based on the triplicate measurements; a high precision of the EDS method was verified in a previous study [24]. The water content and possible carbonation were investigated by thermogravimetric analysis and derivative thermogravimetry (TGA-DTG) using a Mettler Toledo TGA/SDTA 851e instrument. A heating rate of 20 °C min^{-1} from 30 to 980 °C was set and N$_2$ was used as the protective gas. In order to unify the content of physically adsorbed water on the zeolites, the powdered zeolites were pre-equilibrated in the humidity- and CO$_2$- controlled desiccator described above for at least one week. Bond variations of the zeolites were characterized by Fourier transformed infrared (FT-IR) spectroscopy in the mid-region (the wavenumber from 3996 to 339 cm^{-1}), which signal was collected by a Bruker Tensor 27 FT-IR spectrometer using the attenuated total reflection (ATR) technique. The relatively flat surface of a small amount of pressed zeolite powder was measured. After subtracting the background signal, the spectrum was normalized by the maximum absorbance of asymmetrical stretch of Si-O(Si/Al) bonds.

2.3. Batch dissolution experiments

Batch dissolution experiments were conducted by dispersing each type of zeolite into ultrapure water at an identical solid-to-liquid (S/L) ratio of 50 g L^{-1}. To study the relationship between solubility products (K$_{sp}$) and temperatures and thus to determine the thermodynamic properties of the zeolite, four temperatures, i.e., 20, 50, 60, and 80 °C, were investigated in batch experiments for each zeolite. Previous kinetic experiments [24] indicated that an approximate equilibrium can be reached within 30 days. After 30 days of equilibration, the suspensions were filtered through 0.22 μm syringe Nylon filters. On the same day, the filtrate from each reactor was divided into two portions for separately measuring pH and aqueous ion concentrations. The pH was measured at ~25 °C using a Knick pH meter (pH-Meter 766, equipped with a Knick SE100 electrode), immediately after the calibration by standard pH buffer solutions at pH 7.00, 10.01, and 12.00. Ion chromatography (IC, Dionex DP series ICS-3000) was employed to quantify the aqueous concentrations of K, Na, Ca, Si and Al ions. An experimental detection limit of 0.025 mg/L and a concentration error of 10% were estimated for the IC measurement.

2.4. Thermodynamic calculations

The activity of a species i, {i}, was calculated from the measured total concentration, m$_i$ (in mol kg^{-1} H$_2$O), using {i} = γ$_i$·m$_i$, where γ$_i$ is
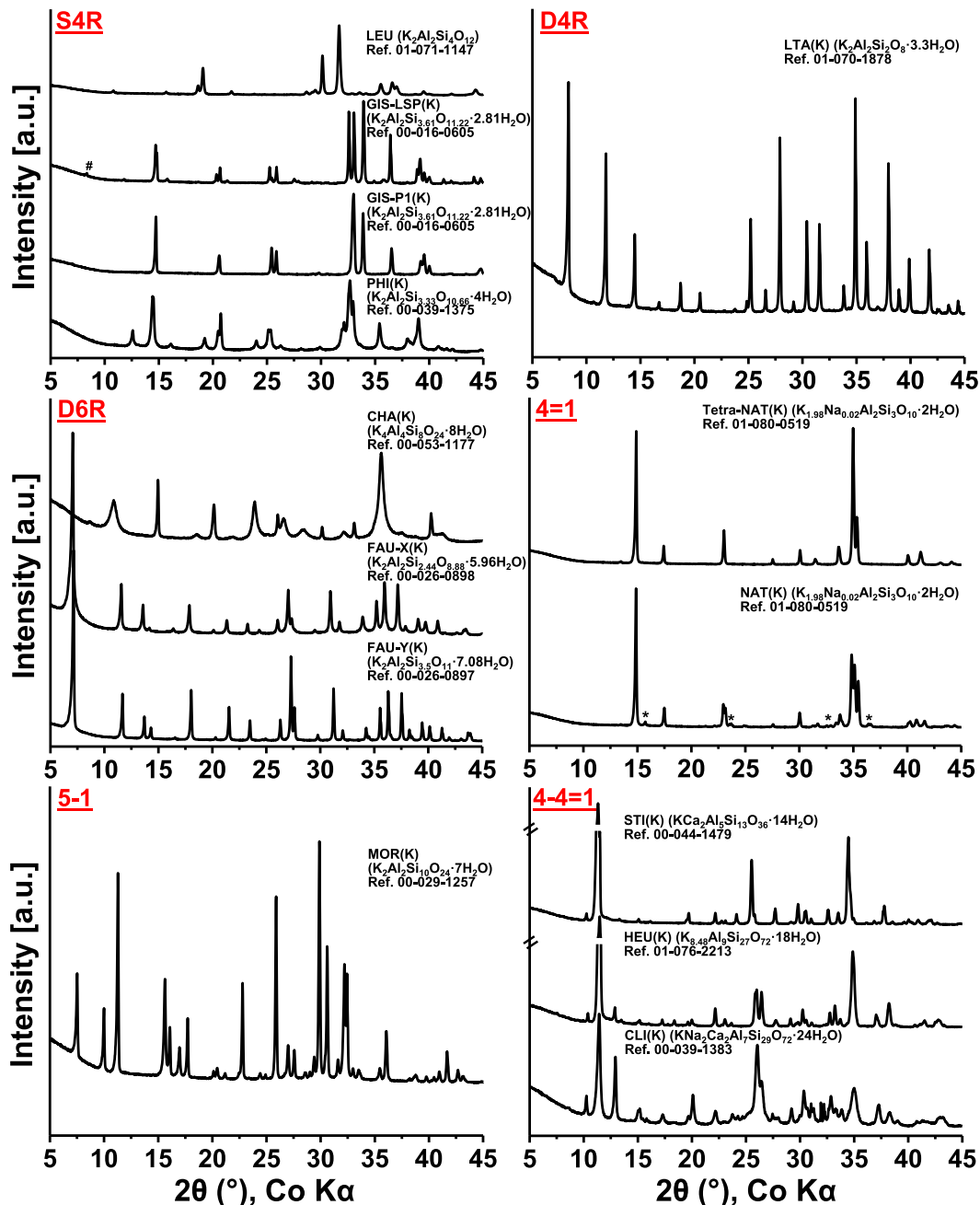
Fig. 1. Powder XRD patterns of the K-based zeolites. The patterns are grouped according to the secondary building unit (SBU, including S4R, D4R, D6R, 4 = 1, 5-1, and 4-4 = 1) that is shown on the top left of each subfigure. For each pattern, the identified phase composition with PDF reference card number is attached on the top right. Only the diffraction peaks of impurities are marked with #: LTA ($K_2Al_2Si_2O_8\cdot3.3H_2O$, Ref. 01-070-1878) and *: K-doped natrolite ($Na_{15.62}K_{0.46}Al_{16}Si_{24}O_{80}\cdot15.36H_2O$, Ref. 01-089-8594), while all the other peaks are from the pure target zeolites.

the activity coefficient using the Gibbs free energy minimization program GEM-Selektor v3.3 [37]. Extended Debye-Hückel equation, applicable up to ~1 M ionic strength [38], was employed to compute the γ_i value:

$$log\gamma_i = \frac{-A_y z_i^2 \sqrt{I}}{1 + B_y a_i \sqrt{I}} + b_y I \tag{1}$$

where the ion size parameter $a_i = 3.67$ Å is assigned a common value for all charged ions and $b_y = 0.123$ in KOH solutions at 25 °C, z_i denotes the charge of species i, I is the effective molal ionic strength (M), and A_y and B_y are P,T-dependent coefficients [38]. The activity of water is directly calculated from its mole fraction: $log\,\gamma_{H2O} = log\,(x_{H2O,w}\,/\,X_w)$, where X_w

is the total mole quantity of the aqueous phase (including water-solvent).

Based on the activities of aqueous species (i.e., {K^+}, {Na^+}, {Ca^{2+}}, {AlO_2^-}, {SiO_2^0}, and {H_2O}) and on the corresponding stoichiometric composition of each zeolite, the solubility products (K_{sp}) at 20, 50, 60, and 80 °C can be calculated out. The standard Gibbs free energy of formation, $\Delta_f G^0$ (in J/mol), can be obtained from the following relationship with K_{sp} at 25 °C:

$$\Sigma_i \nu_i \Delta_f G_i^0 = \Delta_r G^0 = -RT ln K_{sp} \tag{2}$$

where ν_i represents the stoichiometric reaction coefficient, $\Delta_f G_i^0$ refers to $\Delta_f G^0$ of the species (including the zeolite phase) used in the dissolution

Table 1

Elemental compositions (in atomic percentage, at.%) of the K-based zeolites. For each zeolite, Cat/Al and Si/Al represent the molar ratios of the charge number of extra-framework cations to Al and of Si to Al, respectively.

Zeolite	SBU	Framework	Na at.%	Al at.%	Si at.%	K at.%	Mg at.%	Ca at.%	Cat/Al	Si/Al
LEU	S4R	ANA	1.07	7.79	13.97	6.31			0.95	1.79
GIS-LSP(K)		GIS		13.93	14.89	13.65			0.98	1.07
GIS-P1(K)		GIS		8.58	12.20	8.31			0.97	1.42
PHI(K)		PHI		6.71	13.92	7.19			1.07	2.07
LTA(K)	D4R	LTA		10.02	10.48	9.26			0.92	1.05
CHA(K)	D6R	CHA		9.94	19.93	10.23			1.03	2.01
FAU-X(K)		FAU		9.15	11.59	8.30			0.91	1.27
FAU-Y(K)		FAU		7.90	14.65	7.29			0.92	1.85
tetra-NAT(K)	4 = 1	NAT		8.40	12.60	7.80			0.93	1.50
NAT(K)		NAT	0.87	11.77	18.01	10.17			0.94	1.53
MOR(K)	5-1	MOR		3.44	28.65	3.63			1.05	8.33
STI(K)	4-4 = 1	STI		7.54	23.37	7.25		0.05	0.98	3.10
HEU(K)		HEU		7.64	23.40	6.95		0.15	0.96	3.06
CLI(K)		HEU	0.12	5.31	26.17	4.60	0.08	0.05	0.94	4.93
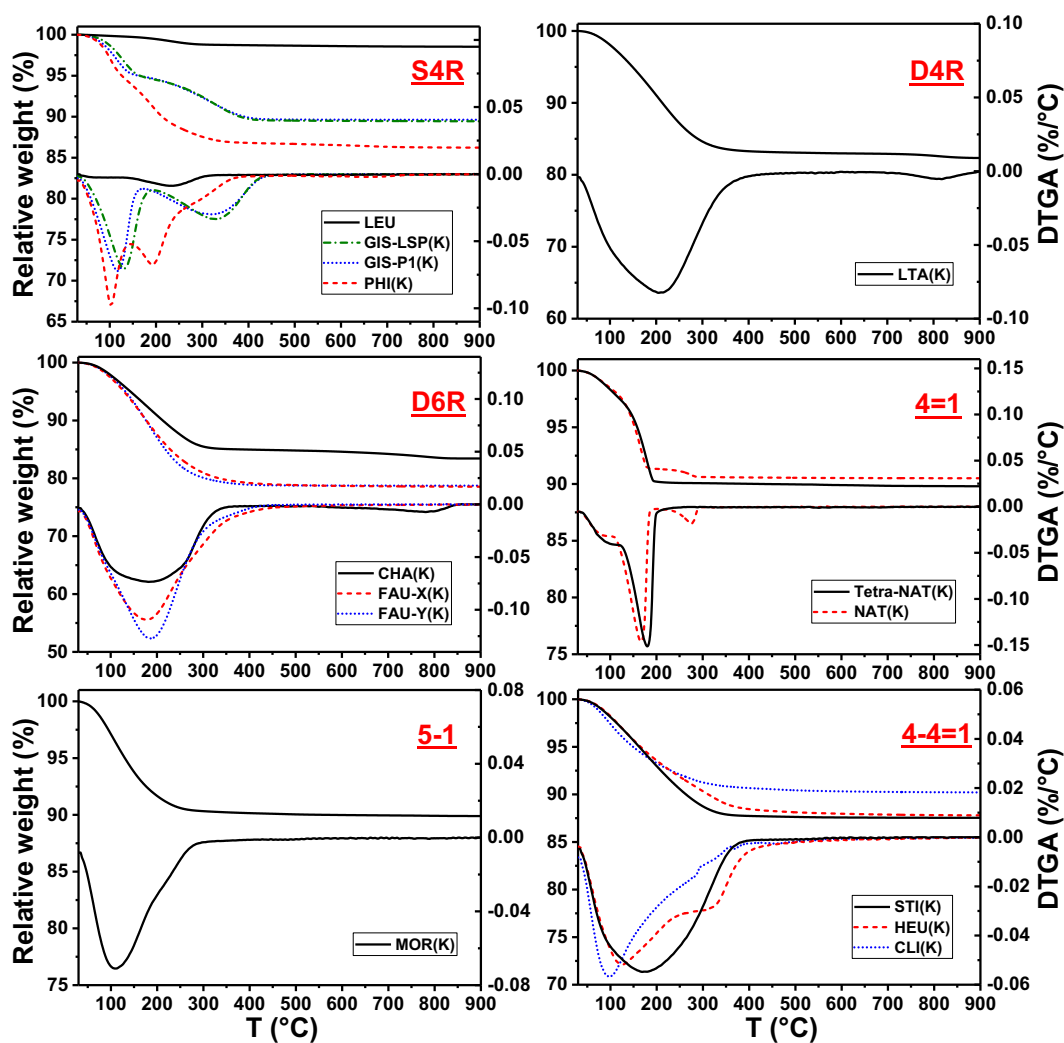
Fig. 2. TGA-DTG curves of the synthesized K-based zeolites. In each graph, curves in the top-half are from TGA results and those in the bottom-half are from DTG results.

reaction and determines the standard Gibbs free energy of reaction, $\Delta_r G^0$. The gas constant R is equal to 8.31451 J/mol/K and T is absolute temperature in K.

Over the narrow temperature interval studied (20–80 °C), where the standard heat capacity, C_P^0 in J/mol/K, can be considered as constant

[39], the apparent Gibbs free energy of formation, $\Delta_a G_T^0$ (in J/mol), referring to standard Gibbs energies of elements at 298.15 K, can be described using:

Table 2

Summary of the TGA-DTG results. The theoretical relative weight loss was calculated and listed only in the case where the EDS data matched well with the XRD result for each zeolite.

Zeolite	Theoretical relative weight loss	Experimental relative weight loss/ DTGA peak position	Number of water determined/ confirmed by TGA
LEU ($K_2Al_2Si_4O_{12}$)	0%	1.24%/235 °C	0
GIS-LSP(K) ($K_2Al_2Si_2O_8\cdot xH_2O$)	–	10.5%/131, 326 °C	2
GIS-P1(K) ($K_{1.67}Al_{1.67}Si_{2.33}O_8\cdot xH_2O$)	–	10.3%/119, 318 °C	1.9
PHI(K) ($K_{2.5}Al_{2.5}Si_{5.5}O_{16}\cdot xH_2O$)	–	13.4%/103, 192 °C	5
LTA ($K_2Al_2Si_2O_8\cdot 3.3H_2O$)	15.8%	16.8%/214 °C	3.3
CHA(K) ($K_2Al_2Si_4O_{12}\cdot 4H_2O$)	14.3%	14.9%/182 °C	4
FAU-X(K) ($K_{2.03}Al_{2.03}Si_{2.47}O_9\cdot 6.04H_2O$)	23.8%	21.1%/176 °C	6.04
FAU-Y(K) ($K_{2.18}Al_{2.18}Si_{3.82}O_{12}\cdot 7.72H_2O$)	23.9%	21.2%/186 °C	7.72
tetra-NAT(K) ($K_2Al_2Si_3O_{10}\cdot 2H_2O$)	8.74%	9.89%/180 °C	2
NAT(K) ($K_2Al_2Si_3O_{10}\cdot 2H_2O$)	8.79%	9.40%/167, 276 °C	2
MOR(K) ($K_{0.65}Al_{0.65}Si_{5.35}O_{12}\cdot xH_2O$)	–	9.84%/109 °C	2.3
STI(K) ($K_{2.2}Al_{2.2}Si_{6.8}O_{18}\cdot xH_2O$)	–	12.3%/168 °C	4.8
HEU(K) ($K_{2.22}Al_{2.22}Si_{6.78}O_{18}\cdot xH_2O$)	–	11.9%/126, 303 °C	4.7
CLI(K) ($K_{1.01}Al_{1.01}Si_{4.99}O_{12}\cdot xH_2O$)	–	9.51%/99 °C	2.3

$$\Delta_a G_T^0 = \Delta_f G_{T_0}^0 - S_{T_0}^0 (T - T_0) - C_p^0 \left(T ln \frac{T}{T_0} - T + T_0 \right) \quad (3)$$

where S^0 is the standard entropy in J/mol K and $T_0 = 298.15$ K. A more detailed description of the derivation of the dependence of the Gibbs free energy on temperature is given in [17,40].

Besides,

$$\Delta_r G_T^0 = \Delta_r H_T^0 - T \Delta_r S_T^0 \quad (4)$$

The S^0 values for the zeolites were selected preferentially from experimentally measured data in literatures if available for identical frameworks and comparable compositions; otherwise, S^0 values were determined independently by fitting the log K_{sp} data as a function of temperature. For C_p^0 values, the first priority was also given to the experimental data reported previously. If not available, they were calculated using the additivity method [16–18] based on reported experimental C_p^0 value of zeolites with the same framework and/or using the elementary (hydro)oxide components assuming $\Delta C_{p,r} = 0$. Thermodynamic data of the elementary (hydro)oxide components (i.e., NaOH, Ca(OH)$_2$, KOH, Al(OH)$_3$, and SiO$_2$) used in the additivity method were extracted from [41,42] and summarized in Table A2. Zeolitic H$_2$O, rather than free H$_2$O, was adopted in the calculation, with S^0 and C_p^0 values of 59.0 and 47.7 J/mol/K, respectively [18]. The molar volumes (V^0, in cm^3/mol) of zeolites were calculated from the indexed PDF cards that matched well with our experimental XRD data. Differences in compositions and the effect it may have on V^0 values were corrected.

Thermodynamic properties, including K_{sp}, ΔG_f^0, ΔH_f^0, S^0, and C_p^0, of the zeolites were modelled and computed using the Gibbs free energy minimization program GEM-Selektor v3.3 [37], together with the built-in PSI/Nagra chemical thermodynamic database [43] for general thermodynamic data of aqueous, solid, and gaseous species. To draw the predominance diagrams for the cement-zeolite-clay system, the PHREEQC (Version 3) [44] and PhreePlot codes (Version 1) [45], based on the PHREEQC database version of the cement database Cemdata18 [25], the thermodynamic data for clay minerals in the THERMOCHIMIE database [26], and the currently generated thermodynamic data for zeolites, were employed. The "hunt and track" algorithm (i.e., ht1) was used for finding field boundaries of most abundant minerals. Note that the thermodynamic data and the dependent species in Cemdata18 and in THERMOCHIMIE are not fully consistent. To minimize inconsistencies, the expressions of species (e.g., AlO$_2^-$ and SiO$_2$) as defined in Cemdata18 were applied identically.

3. Results and discussion

3.1. Characterizations of zeolites

3.1.1. Zeolite frameworks and SBUs

In zeolitic structures, SiO$_4$ and AlO$_4$ tetrahedra, the so-called primary building units, constitute a wide range of small ring structures (i.e., SBUs), which further connect with each other and form various long-range aluminosilicate frameworks. These long-range orders in structures are quite sensitive to XRD. As illustrated in Figs. 1, 10 types of frameworks (i.e., ANA, GIS, PHI, LTA, CHA, FAU, NAT, MOR, STI, and HEU) belonging to six SBU groups (i.e., S4R, D4R, D6R, 4 = 1, 5-1, and 4-4 = 1) were recognized in the K-based zeolites studied. Except for GIS-LSP(K) and NAT(K), no obvious diffraction peak indicating the presence of an impurity was observed in the XRD patterns, confirming that most of the obtained K-based zeolites were highly pure. Only in GIS-LSP(K), a tiny amount of LTA(K) was detected, which is a K$^+$-exchange product from the original by-product (i.e., LTA(Na)) used in GIS-LSP(Na) synthesis [24]. In NAT(K), the small impurity peaks were attributed to a K-doped natrolite (Na$_{15.62}$K$_{0.46}$Al$_{16}$Si$_{24}$O$_{80}\cdot15.36$H$_2$O), that was newly formed during the cation exchange experiment.

Natrolite has ordered Si/Al tetrahedral sites (T-sites) in orthorhombic symmetry, which is different from tetranatrolite that has completely disordered T-sites in tetragonal symmetry [34]. The atomic structure difference between tetranatrolite and natrolite are visible by the almost complete split of XRD peaks at ~22.3, 23.5, 25.0, 32.5, and 36.5° 2θ in the case of natrolite [24]. After K$^+$ exchange, the XRD peak splits in the case of NAT(K), as shown in 4 = 1 group in Fig. 1, can be still observed clearly, indicating that NAT(K) has a well ordered T-sites distribution and a highly crystalline structure. These factors might contribute to the retention of the tiny amount of original Na$^+$ and thus to the formation of a small quantity of K-doped natrolite.

In the S4R group, GIS-LSP(K), GIS-P1(K) and PHI(K) showed similar XRD peak positions and relative intensities. Similarity was also observed in D6R, 4 = 1, and 4-4 = 1 groups, indicating that the short-range order (characterized by the SBU) strongly affects the long-range order (e.g., the framework type that is sensitive to XRD analysis). In contrast to other zeolites, both LEU and NAT(K) showed large difference from their Na-endmembers [24] in XRD patterns. After K$^+$ exchange, analcime (ANA) loses all the structural water in the cage and transforms to its anhydrous K-endmember, LEU. Although analcime and leucite have the same framework (ANA type) and space group ($I4_1/a$), their XRD patterns are largely different, suggesting that the water loss influences the cage structure. In comparison, NAT(K) and NAT contain the same amount of structural water and thus the large difference in XRD patterns mainly result from the different cations in the cages. Only small difference in the XRD patterns were observed in the cases of GIS, PHI, LTA, CHA, FAU, MOR, STI, and HEU frameworks, possibly indicating that these zeolitic cages/channels might be more accessible and that the cage cations be more exchangeable.

As discussed above, generally the framework types of zeolites can be easily identified by XRD. However, in some cases, zeolites having the same framework but different Si/Al ratios, e.g., GIS-LSP(K) vs. GIS-P1 (K) and FAU-X(K) vs. FAU-Y(K), give nearly indistinguishable XRD patterns, due to minor differences in positions and/or intensities. Thus,
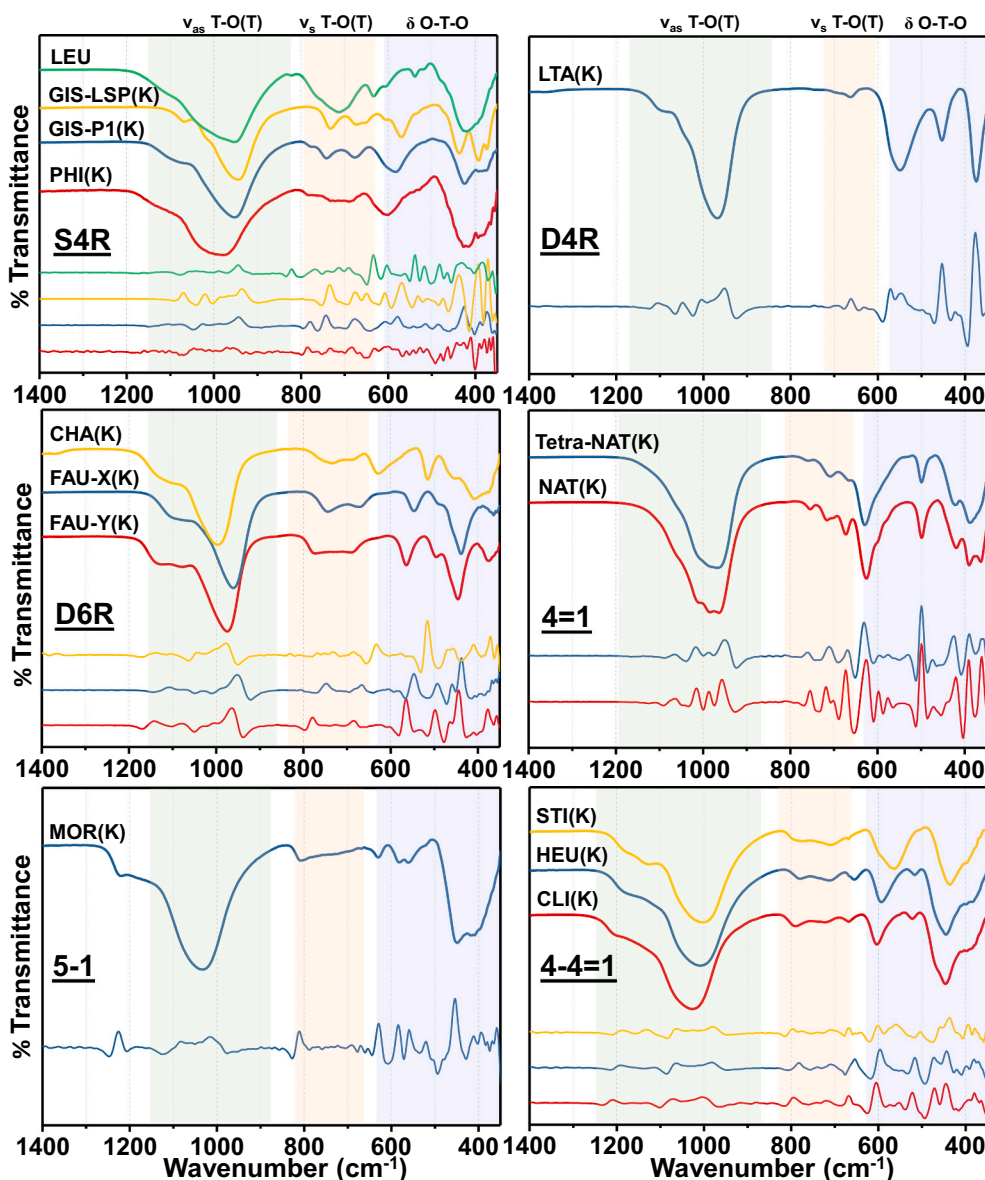
Fig. 3. FTIR transmittance spectra and the corresponding 2nd derivative spectra (as plotted at the bottom of each subfigure in the correspondingly identical color) of each SBU group of K-based zeolites.

an analysis of the elemental composition is required for validating the XRD results.

3.1.2. Elemental composition

The bulk elemental composition (atomic number ≥ 11) of each zeolite was determined by SEM-EDS and listed in Table 1. In alumino-silicate zeolites, the negatively charged sites in the framework, which is caused by the substitution of Si^{4+} sites by Al^{3+}, should be balanced by the extra-framework cations. Thus, the molar ratio of the charge of extra-framework cation(s) to Al, denoted with Cat/Al, is theoretically equal to one [27]. As shown in Table 1, all the Cat/Al values are quite close to one, verifying that the bulk elemental compositions were reliably determined by the SEM-EDS method. Most of the K^+-exchanged zeolites contained only K^+ as the extra-framework cation. In LEU and NAT(K) a small amount of the original Na^+ was still present., Similarly, the K^+-exchanged natural zeolites, i.e., STI(K), HEU(K) and CLI(K), contained a tiny amount of other cations (e.g., Na^+, Mg^{2+}, and Ca^{2+}). For LEU, a control experiment was conducted by making three more exchange cycles with K^+ and the K^+-exchange product was

characterized by EDS as well, showing that the content of Na^+ remained constant, which suggests that the retained Na^+ in LEU is strongly trapped in the cage and not exchangeable with K^+. The small percentage of Na in NAT(K) is expected to originate from the K-doped natrolite ($Na_{15.62}K_{0.46}Al_{16}Si_{24}O_{80}\cdot15.36H_2O$) observed by XRD.

The Si/Al ratios obtained from SEM-EDS (see Table 1) of GIS-LSP(K), LTA(K), CHA(K), FAU-X(K), FAU-Y(K), tetra-NAT(K), and NAT(K) are nearly identical with the corresponding values derived from the XRD results based on referenced zeolites. However, the Si/Al ratio of LEU was determined to be ~1.8, which is slightly lower than the Si/Al of 2.0 expected by XRD analysis. The slightly lower Si/Al ratio was also observed in previous studies [46], where a similar hydrothermal cation exchange method has been used for leucite synthesis. GIS-P1(K) and GIS-LSP(K) resulted in similar XRD patterns, whereas GIS-P1(K) had a higher Si/Al ratio of ~1.42 than GIS-LSP(K) (Si/Al ratio ~1.07) as determined by EDS. PHI(K) had a Si/Al ratio of ~2.07, which is higher than the 1.665 based on the XRD result but matched well with Si/Al of the original phillipsite (i.e., PHI(NaK)) [24] prior to K^+ exchange. Considering that the cation exchange process should not change Si/Al ratios

Table 3
Summary of the vibration peak wavenumbers (cm^{-1}) of FTIR spectra for the K-based zeolites.[a]

SBU group	Zeolite	ν O—H	δ O—H	ν$_{as}$ T—O(T) — Ex	ν$_{as}$ T—O(T) — In	ν$_s$ T—O(T) — Ex	ν$_s$ T—O(T) — In	Ring — Ex	δT—O — In	Pore — Ex
S4R	LEU	–	–	1117	1043, 945	822, 766	714, 690	633, 604, 538, 517	482, 465, 432	
	GIS-LSP(K)	3392, 3225	1653	1070	1020, 960, 935	733	675, 650	607, 569, 532	438	393, 372
	GIS-P1(K)	3609, 3408	1632	1105	1026, 943	779, 742	677	608, 579	424	390, 374
	PHI(K)	3618, 3371	1636	1136	1045, 970	785, 733	690	602, 526	428	
D4R	LTA(K)	3385, 3279	1657	1105	1047, 1005, 951		662	550	453	374
D6R	CHA(K)	3587, 3406, 3226	1639	1138, 1103	1043, 1005, 978	768, 731	685	633, 515	469, 457	409, 370
	FAU-X(K)	3391, 3242	1647	1107	1028, 987, 953	748	665	548	494, 459, 438	
	FAU-Y(K)	3396, 3236	1647	1142, 1078	1028, 1005, 964	779	685	565	498, 465, 444	378, 357
4 = 1	Tetra-NAT (K)	3598, 3440, 3226	1618	1066	1016, 987, 951	760	712, 669	631, 596, 577, 530	499, 424	390, 361
	NAT(K)	3572, 3394, 3230	1618	1064	1014, 987, 956	754	717, 702, 673	627, 598, 577	499, 472, 420	391, 361
5-1	MOR(K)	3433	1635	1084, 1059	1226, 1038, 1016	812		629, 584, 559, 521	455, 411	395
4-4 = 1	STI(K)	3589, 3419, 3222	1652, 1635	1130, 1064	1188, 980	796, 775, 739	710, 669	602, 559, 503	459, 438	395, 378
	HEU(K)	3595, 3427, 3259	1653, 1635	1113, 1063	1192, 982	783, 740	710, 654	596, 517	472, 444	397, 380, 370
	CLI(K)	3630, 3444, 3221	1653, 1635	1132, 1070	1209, 1005	794, 740	721, 667	606, 573, 553, 523	470, 445	391, 380, 364

[a] ν$_{as}$, asymmetric stretching vibrations; ν$_s$, symmetric stretching vibrations; δ, bending vibrations; T, Si/Al tetrahedron; Ex, external linkage; In, internal tetrahedra; Ring, ring vibrations; Pore, pore opening vibrations.

largely and a perfectly matching reference PDF card of XRD analysis may be still missing for the PHI(K), the Si/Al ratio of 2 was accepted in this study. Since MOR(K), STI(K), HEU(K), and CLI(K) typically have high and variable Si/Al ratios [27], which is difficult to assess based on XRD, their ratios obtained by EDS analysis were adopted.

3.1.3. Water content and possible carbonation

TGA-DTG analysis was performed to quantify the structural water content as well as to check any possible contamination or carbonation during the synthesis. As shown in Fig. 2, the zeolites were grouped and plotted based on the SBU. Overall, no significant carbonation was observed. Only for LTA(K) and CHA(K), tiny DTG peaks at ~800 °C occurred, indicating slight carbonation.

The quantitative TGA-DTG results are summarized in Table 2. All weight loss below ~500 °C was attributed to water loss. In the S4R group, LEU resulted in a negligible water loss (1.24%), matching well with the chemical formula of $K_2Al_2Si_4O_{12}$ identified by XRD. For GIS-LSP(K), GIS-P1(K), and PHI(K), their Si/Al ratios derived from EDS analysis were inconsistent with those from XRD measurements and thus their theoretical relative weight losses were unknown. The same cases were also met with MOR(K), STI(K), HEU(K), and CLI(K). GIS-LSP(K) and GIS-P1(K) showed very similar DTG curves, giving two characteristic water loss peaks at ~125 and ~322 °C. Compared to the Na-endmember (16.3% relative weight loss at 121, 221, and 288 °C) [24], GIS-LSP(K) had a slightly higher water loss temperature and a lower water content (i.e., 10.5% at 131 and 326 °C). As Na^+ is more hydrophilic than K^+ and can attract more water molecules [47], the K-endmember are expected to contain less water than the Na-endmember for zeolites having the same framework type and similar Si/Al ratios. Indeed, lower water content was confirmed for PHI(K), LTA(K), CHA(K), FAU-X(K), FAU-Y(K), and MOR(K), compared to the corresponding values of 17.1%, 20.7%, 20.2%, 24.5%, 25.1%, and 11.5% in the Na-based cases [24]. In addition, the DTG pattern of PHI(K) was shifted to higher temperatures than that of PHI(Na), indicating that the water structure in the cages is different and thus the corresponding extra-framework sites for K^+ differ from those for Na^+ in PHI zeolites.

For LTA(K) in the D4R group, the DTG peak of dehydration was located at approximately the same temperature, ~200 °C, as LTA(Na) but was much broader, suggesting a more disordered water structure in LTA(K). In contrast, the K^+-exchange did not bring significant changes to the TGA/DTG curves of the D6R zeolites (i.e, CHA, FAU-X, and FAU-Y), except for the lower water contents of their K-endmembers mentioned above.

In the 4 = 1 group, tetra-NAT(K) and NAT(K) showed the similar water losses below 200 °C, whereas NAT(K) lost a further ~0.7% relative weight at 276 °C. This signal is probably originating from the small amount of poorly K^+-exchanged NAT observed by XRD, as Na-containing has a characteristic water loss between 205 and 350 °C [24]; note that the "peak" position of DTG shifted to apparently lower temperatures if only a small quantity is present [48]. MOR(K) in the 5-1 group had a similar TGA/DTG curve but a lower water content compared with MOR(Na).

In the 4-4 = 1 group, all three K-based zeolites were obtained from natural zeolites, in which Ca^{2+} originally predominated. As shown in Table 2, their K-endmembers contained less structural water in the cages than the Ca-dominant forms [10]. Aqueous K^+ and Ca^{2+} are approximately hydrated with 3 and 6 water molecules, respectively [47]. Taking into account the two times difference in the charge, K^+ and Ca^{2+} should bring nearly equivalent water content via compensating the same amount of negative charge of the aluminosilicate framework. As K^+ is expected to occupy two times the extra-framework sites occupied by Ca^{2+}, the higher water content in the Ca^{2+} case could result from the extra water molecules existing in the vacant cages/channels. STI(K) displayed a very broad water loss peak at 168 °C in the DTG curve, which largely differed from the features of the original natural stilbite (Ca) [10], indicating that the presence of K^+ led to a more disordered water structure in STI zeolites. Regarding HEU(K), the thermogravimetric characteristic of heulandite, resulting in a well-defined DTG peak at ~310 °C [10,49], can be still observed. In contrast, the TGA/DTG curve of CLI(K) remained nearly the same as that of the original Ca-containing clinoptilolite [10].

The number of water molecules in the chemical formula was

Table 4

Solution composition and pH of zeolite dissolution experiments at 20, 50, 60, and 80 °C. Experimental log K_{sp} values were calculated and listed. A general error of 3% was applied on the log K_{sp} values.[a]

Zeolite	T °C	pH[b]	[Na]$_{tot}$ mM	[K]$_{tot}$ mM	[Ca]$_{tot}$ mM	[Si]$_{tot}$ mM	[Al]$_{tot}$ mM	log K_{sp}[c]
LEU	20	9.94	0.0478	1.1469	bdl	0.3222	0.5199	−27.81 ± 0.83
	50	9.46	0.4600	2.4374	bdl	0.4937	1.4418	−25.52 ± 0.77
	60	9.45	0.7971	2.8904	bdl	0.6296	1.5635	−25.14 ± 0.75
	80	9.49	1.3328	4.3314	bdl	1.0938	2.2203	−24.16 ± 0.72
GIS-LSP(K)	20	9.49	0.0070	1.2734	bdl	0.3875	0.8181	−19.16 ± 0.57
	50	8.82	0.0477	3.1792	bdl	0.1148	1.8730	−18.64 ± 0.56
	60	8.69	0.0704	4.0299	bdl	0.2303	2.3548	−17.64 ± 0.53
	80	8.45	0.0888	5.4130	bdl	0.3029	3.5292	−16.80 ± 0.50
GIS-P1(K)	20	10.52	0.0055	1.1168	bdl	0.2057	0.2500	−21.29 ± 0.64
	50	9.32	0.0055	1.6538	bdl	0.2084	0.3446	−19.66 ± 0.59
	60	9.15	0.0076	1.8958	bdl	0.2429	0.3944	−19.26 ± 0.58
	80	8.77	0.0074	2.5160	bdl	0.3007	1.0638	−17.97 ± 0.54
PHI(K)	20	10.52	0.0026	1.9437	bdl	0.0910	0.0648	−43.61 ± 1.31
	50	9.47	0.0045	3.2809	bdl	0.1916	0.1348	−38.26 ± 1.15
	60	9.22	0.0053	3.4261	bdl	0.2357	0.1470	−37.26 ± 1.12
	80	8.81	0.0050	3.9804	bdl	0.3804	0.2549	−34.92 ± 1.05
LTA(K)	20	9.11	0.0110	2.3131	bdl	0.1256	0.2337	−20.56 ± 0.62
	50	8.47	0.0188	6.0681	bdl	0.1390	0.7670	−18.63 ± 0.56
	60	8.43	0.0274	7.4236	bdl	0.1487	0.8590	−18.32 ± 0.55
	80	8.27	0.0272	9.4408	bdl	0.3048	3.2156	−16.38 ± 0.49
CHA(K)	20	8.05	0.0053	4.0011	bdl	0.0327	0.0204	−32.28 ± 0.97
	50	7.09	0.9347	11.2612	bdl	0.0486	0.0421	−30.19 ± 0.91
	60	6.94	0.9925	12.4547	bdl	0.0579	0.0534	−29.61 ± 0.89
	80	6.69	1.3265	12.8429	bdl	0.1092	0.1440	−27.64 ± 0.83
FAU-X(K)	20	9.58	0.0146	1.3024	bdl	0.1471	0.6791	−22.26 ± 0.67
	50	8.71	0.0340	2.4181	bdl	0.1827	1.2130	−20.76 ± 0.62
	60	8.60	0.0399	2.7835	bdl	0.1901	1.4177	−20.47 ± 0.61
	80	8.30	0.0439	3.8721	bdl	0.3745	2.8336	−18.82 ± 0.56
FAU-Y(K)	20	8.55	bdl	0.3922	bdl	0.0707	0.0922	−32.20 ± 0.97
	50	7.92	0.0016	0.7729	bdl	0.1631	0.1419	−29.77 ± 0.89
	60	7.72	0.0018	0.8931	bdl	0.2010	0.1892	−29.01 ± 0.87
	80	7.51	0.0025	1.0230	bdl	0.4332	0.4747	−26.75 ± 0.80
tetra-NAT(K)	20	10.07	0.0079	1.2674	bdl	0.2298	0.1715	−25.52 ± 0.77
	50	8.94	0.0114	1.7686	bdl	0.3469	0.3433	−23.27 ± 0.70
	60	8.44	0.0131	2.0307	bdl	0.2876	0.4308	−23.00 ± 0.69
	80	8.24	0.0188	2.4317	bdl	0.6194	0.7467	−21.37 ± 0.64
NAT(K)[d]	20	8.91	0.0225	0.4230	0.0131	0.2319	0.0797	−26.02 ± 0.78
	50	7.54	0.0399	0.7912	bdl	0.2524	0.1519	−24.74 ± 0.74
	60	7.43	0.0496	0.9614	bdl	0.2918	0.2070	−24.12 ± 0.72
	80	7.51	0.0697	1.1560	bdl	0.5612	0.5619	−22.25 ± 0.67
MOR(K)	20	10.27	0.0012	1.8161	0.0138	1.6069	0.0045	−23.13 ± 0.69
	50	9.14	0.0016	3.6253	bdl	2.8281	0.0053	−19.67 ± 0.59
	60	9.02	0.0018	4.2135	bdl	3.7584	0.0073	−18.86 ± 0.57
	80	8.72	0.0024	5.5943	bdl	5.2358	0.0143	−17.68 ± 0.53
STI(K)	20	7.66	bdl	0.3228	bdl	0.0940	0.0038	−47.11 ± 1.41
	50	6.99	bdl	0.6148	bdl	0.3959	0.0176	−40.85 ± 1.23
	60	6.86	bdl	0.6830	bdl	0.5338	0.0341	−39.24 ± 1.18
	80	6.75	bdl	0.7138	bdl	0.7266	0.2317	−36.43 ± 1.09
HEU(K)	20	7.92	bdl	0.2030	bdl	0.1073	0.0104	−46.28 ± 1.39
	50	7.10	bdl	0.5318	bdl	0.4020	0.0233	−40.74 ± 1.22
	60	6.93	bdl	0.6091	bdl	0.5367	0.0416	−39.21 ± 1.18
	80	6.82	bdl	0.5334	bdl	0.7627	0.2183	−36.68 ± 1.10
CLI(K)	20	7.99	bdl	0.4045	bdl	0.2822	0.0010	−27.24 ± 0.82
	50	7.14	bdl	0.7012	bdl	0.7688	0.0021	−24.55 ± 0.74
	60	6.94	bdl	0.8101	bdl	1.0754	0.0023	−23.71 ± 0.71
	80	6.60	bdl	0.7661	bdl	1.7670	0.0081	−22.12 ± 0.66

[a] bdl: below detection limit that was approximately 0.025 mg/L for each element; [Mg]$_{tot}$ was determined as well but below detection limit for all samples.

[b] pH was measured at laboratory temperature (25 °C) and corrected to 20 °C, 50 °C, 60 °C and 80 °C. The pH differences caused by the temperature differences were calculated with GEMS; the measured pH values above 8 were corrected +0.16 for 20 °C, −0.74 for 50 °C, −0.98 for 60 °C, and −1.40 for 80 °C.

[c] log K_{sp} values refer to K^+, AlO_2^-, SiO_2^0 and H_2O; detailed dissolution reactions are shown in Table A4.

[d] The log K_{sp} values of the K-doped natrolite ($Na_{1.94}K_{0.06}Al_2Si_3O_{10}\cdot1.92H_2O$) at 20 °C, 50 °C, 60 °C and 80 °C were determined to be −28.57, −27.34, −26.70, and −24.69, respectively.

calculated based on the relative weight loss of water (Table 2) and used in the following thermodynamic study.

3.1.4. FT-IR analyses

The FT-IR transmittance spectra and the corresponding 2nd derivative spectra, with the wavenumber ranging from 1400 to 340 cm^{-1}, of each SBU group of K-based zeolites are shown in Fig. 3. The FT-IR spectra below 1400 cm^{-1} clearly exhibit the vibration features of the aluminosilicate frameworks of zeolites while the spectra between 4000 and 1250 cm^{-1} mainly displayed the stretching (ν O—H) and bending (δ O—H) vibration bands of H—O—H (in H_2O). As shown in Fig. A1 and Table 3, ν O—H and δ O—H typically resulted in a broad peak envelop (except for LEU, which contains hardly any water) centered at ~3350 cm^{-1} and a relatively sharp peak at 1630 cm^{-1}, respectively. The

Table 5

Standard thermodynamic data of K-based zeolites at 25 °C, derived in the current study.

SBU group	Zeolite	log K_{sp}	$\Delta_f G^0$ (kJ/mol)	$\Delta_f H^0$ (kJ/mol)	S^0 (J/mol/K)	C_p^0 (J/mol/K)	V^0 (cm³/mol)
S4R	LEU	-27.60 ± 0.83	-5711.07	-6048.59	360[a]	328[a]	177.35
	($K_2Al_2Si_4O_{12}$)						
	GIS-LSP(K)	-19.60 ± 0.59	-4472.95	-4814.83	364	309[b]	140.26
	($K_2Al_2Si_2O_8 \cdot 2H_2O$)						
	GIS-P1(K)	-21.20 ± 0.64	-4367.11	-4699.80	347	299[b]	140.34
	($K_{1.67}Al_{1.67}Si_{2.33}O_8 \cdot 1.9H_2O$)						
	PHI(K)	-42.60 ± 1.28	-8787.69	-9546.58	598	639[b]	312.19
	($K_{2.5}Al_{2.5}Si_{5.5}O_{16} \cdot 5H_2O$)						
D4R	LTA(K)	-20.50 ± 0.62	-4786.42	-5218.42	365	371[b]	186.82
	($K_2Al_2Si_2O_8 \cdot 3.3H_2O$)						
D6R	CHA(K)	-32.30 ± 0.97	-6686.63	-7228.69	607	564[c]	252.91
	($K_2Al_2Si_4O_{12} \cdot 4H_2O$)						
	FAU-X(K)	-22.50 ± 0.68	-5872.72	-6453.89	618	577[c]	223.48
	($K_{2.03}Al_{2.03}Si_{2.47}O_9 \cdot 6.04H_2O$)						
	FAU-Y(K)	-32.35 ± 0.97	-7619.01	-8374.57	772	745[c]	291.27
	($K_{2.18}Al_{2.18}Si_{3.82}O_{12} \cdot 7.72H_2O$)						
4 = 1	tetra-NAT(K)	-25.27 ± 0.76	-5338.72	-5731.87	416	370[d]	186.51
	($K_2Al_2Si_3O_{10} \cdot 2H_2O$)						
	NAT(K)	-26.35 ± 0.79	-5344.89	-5738.04	416	370[d]	186.51
	($K_2Al_2Si_3O_{10} \cdot 2H_2O$)						
5-1	MOR(K)	-22.00 ± 0.66	-5851.31	-6323.10	346	388[b]	190.87
	($K_{0.65}Al_{0.65}Si_{5.35}O_{12} \cdot 2.3H_2O$)						
4-4 = 1	STI(K)	-45.20 ± 1.36	-9505.55	$-10,301.12$	630[b]	669[b]	316.67
	($K_{2.2}Al_{2.2}Si_{6.8}O_{18} \cdot 4.8H_2O$)						
	HEU(K)	-45.15 ± 1.35	-9487.07	$-10,289.26$	586	665[b]	324.80
	($K_{2.22}Al_{2.22}Si_{6.78}O_{18} \cdot 4.7H_2O$)						
	CLI(K)	-26.80 ± 0.80	-5978.26	-6448.47	378	395[b]	191.26
	($K_{1.01}Al_{1.01}Si_{4.99}O_{12} \cdot 2.3H_2O$)						

All values shown were obtained in the current study except where indicated. log K_{sp} was calculated with respect to the species of AlO_2^-, K^+, SiO_2^0, and H_2O. For the additivity method, the thermodynamic data of the elementary (hydro)oxide components (i.e., zeolitic H_2O, NaOH, $Ca(OH)_2$, KOH, $Al(OH)_3$, and SiO_2) was summarized in Table A2.

[a] Measured by [58].

[b] Calculated using additivity method based on the elementary (hydro)oxide components.

[c] Calculated by additivity method starting from zeolites with the CHA framework [18].

[d] Calculated starting from the NAT framework [59].

vibration peak wavenumbers of the FTIR spectra and the corresponding attributions were summarized in Table 3. As illustrated by Flanigen et al. [50], the IR transmittance bands of zeolite frameworks generally show: 1) internal vibrations of the TO_4 tetrahedra (i.e., SiO_4 or AlO_4), including asymmetrical stretch (ν_{as}) at 1250–920 cm^{-1}, symmetrical stretch (ν_s) at 720–650 cm^{-1}, and T—O bend (δ) at 500–420 cm^{-1}; and 2) external vibrations of linkages, including ν_{as} at 1150–1050 cm^{-1}, ν_s at 820–750 cm^{-1}, ring vibrations at 650–500 cm^{-1}, and pore opening vibrations at 420–300 cm^{-1}.

Overall, zeolites belonging to the same SBU group have quite similar features in the IR spectra (Fig. 3), indicating that the IR bands typically characterize the local structures of the fundamental building units (e.g., SBUs). The FTIR spectra of the K-zeolites had no obvious difference from those of the corresponding Na-endmembers or Ca-endmembers [10,24], except for the case of LEU and NAT(K). The band of leucite in the range 1100–900 cm^{-1}, assigned to asymmetric stretching vibrations of Si—O (Si) and Si—O(Al) bonds, shows an clear shift to lower wavenumbers, compared to ANA [24]. This shift could theoretically result from the weaker electronegativity of K^+ than that of Na^+. However, a similar shift was not observed for the other zeolites, suggesting that the IR bands were not very sensitive to the electronegativity differences between K^+, Na^+, and Ca^{2+} and that this shift in FTIR is rather due to the structural differences between LEU and ANA. The sharp IR peak features in the range of 1100–900 cm^{-1} typical for natrolite, NAT(Na), broaden strongly for NAT(K) after K^+ exchange, indicating that the occupation of K^+ in the extra-framework sites of NAT influences the asymmetric stretching vibrations of T—O(T) bonds. Overall, the main IR bands for each SBU group matched well with our previous works [10,24] and the literatures e.g. [51,52], which confirmed that the targeted K-based zeolites were obtained successfully.

3.2. Thermodynamic properties of K-based zeolites

3.2.1. Solubility products

Based on the combination of XRD, EDS, TGA, and FTIR results presented above, the composition of the zeolite were determined stepwise as shown in Table A3. The solubility of those zeolites, which contained in addition to K^+ also some Na^+ or Ca^{2+}, were calculated assuming the presence of K^+ only and also assuming a solid solution incorporating some Na^+ or Ca^{2+}; as K^+ was the dominating cation the results were nearly identical, as already observed previously for Na and Ca-zeolites [10,24]. The various types of extra-framework cations can be treated as a zeolite solid solution whose solubility product is nearly equal to that of the endmember with the main cation [53,54]. The K^+ endmember forms were adopted (Table A3) in the thermodynamic study. The dissolved $[Na]_{tot}$ and $[Ca]_{tot}$ were always much lower than $[K]_{tot}$ as shown in Table 4, confirming again that the original host cations were almost completely substituted by K^+, in agreement with the EDS results. The only exception was LEU, where a considerable amount of Na^+ was observed; the presence of some Na^+ retained in the zeolite cages was also detected by EDS.

The aqueous concentrations and pH values measured after equilibrium for 30 days in Table 4 were used to calculate log K_{sp} values of each zeolite according to the dissolution reactions shown in Table A4. The general error on the log K_{sp} value was estimated as previously [24] to be 3%. In general, the total element concentrations and the resulting log K_{sp} values (Table 4) of the different zeolites become less negative with temperature, suggesting a positive reaction enthalpy and thus an increase of solubility at higher temperature.

3.2.2. Thermodynamic data of K-based zeolites

The GEMS code was employed to calculate the $\Delta_f G^0$, $\Delta_f H^0$, and S^0 at

Table 6

Thermodynamic properties of zeolites reported in the literature. Experimental values (e.g., derived from solubility experiments and calorimetric measurement) are marked in bold and calculated values are non-bold.

| Zeolite	Formula	log K_{sp} (298.15 K)	ΔG_f^0 kJ/mol	ΔH_f^0 kJ/mol	S^0 J/mol K	C_p J/mol K	Ref
Leucite	$K_2Al_2Si_4O_{12}$				**360.0 ± 2.0**	**327.6 ± 2.0**	[58]
Analcime	$Na_2Al_2Si_4O_{12}\cdot2H_2O$	−33.47	−6177.8	−6616.9	459	425	[8]
	$Na_{1.98}Al_{1.98}Si_{4.02}O_{12}\cdot2H_2O$	−32.00	−6178.1	**−6616.0**	**462**	**425**	[60]
	$Na_2Al_2Si_4O_{12}\cdot2H_2O$	−33.23	−6176.4	−6613.4	469	424	[18]
	$Na_2Al_2Si_4O_{12}\cdot2H_2O$	−34.74	−6192.6	−6624.0			[14]
	$Na_2Al_2Si_4O_{12}\cdot2H_2O$	**−32.12**	**−6178.4**				[23]
	$Na_2Al_2Si_4O_{12}\cdot2H_2O$	**−29.30 ± 0.4**	**−6160.2**				[61]
	$Na_2Al_2Si_4O_{12}\cdot2H_2O$				**468.6 ± 1.2**	**419.8**	[62]
	$Na_2Al_2Si_4O_{12}\cdot2H_2O$	**−26.8 ± 0.8**	**−6139.70**	**−6575.84**	469	425	[24]
Gismondine	$Na_2Al_2Si_2O_8\cdot3.8H_2O$	**−19.6 ± 0.6**	**−4858.72**	**−5314.82**	**374**	384	[24]
	$CaAl_2Si_2O_8\cdot4.5H_2O$	−26.25	−5102.4	−5589.9	371	435	[56]
	$CaAl_2Si_2O_8\cdot4.5H_2O$	−23.17	−5084.8	−5564.6	397	459	[56]
	$CaAl_2Si_2O_8\cdot4.5H_2O$	**−20.30**	**−5057.8**	**−5424.0**	**779**	**753**	[8]
	$CaAl_2Si_2O_8\cdot4.5H_2O$	**−23.5 ± 0.7**	**−5076.03**	**−5527.74**	**491**	435	[10]
Phillipsite	$K_2Al_2Si_6O_{16}\cdot6H_2O$	−45.66	−8920.9	−9683.7	**780**	**702**	[56]
	$Na_{1.08}K_{0.80}Al_{1.88}Si_{6.12}O_{16}\cdot6H_2O$				**771.9 ± 2.4**	**786.2**	[63]
	$Na_{1.5}KAl_{2.5}Si_{5.5}O_{16}\cdot5H_2O$	**−39.9 ± 1.2**	**−8741.26**	**−9461.67**	707	626	[24]
	$Na_2Al_2Si_6O_{16}\cdot6H_2O$	−42.84	−8863.7	−9623.3	**764**	**662**	[56]
	$Na_{2.5}Al_{2.5}Si_{5.5}O_{16}\cdot5H_2O$	**−39.4 ± 1.2**	**−8717.83**	**−9438.72**	692	620	[24]
	$CaAl_2Si_6O_{16}\cdot6H_2O$	−41.10	−8882.7	−9648.0	**684**	**644**	[56]
	$CaAl_2Si_6O_{16}\cdot6H_2O$				**697**	**586**	[18]
LTA	$Na_2Al_2Si_2O_8$		−3899.2	**−4121.7**	**271**	**260**	[64]
	$Na_2Al_2Si_{12}O_{8.24}$	−23.24	−4078.4				[19]
	$Na_{2.0}Al_{2.0}Si_{2.0}O_{8.0}\cdot4.36H_2O$			**−5454.8**			[14]
	$Na_{1.98}Al_{1.98}Si_{2.02}O_8\cdot5.31H_2O$	**−18.2 ± 0.6**	**−5203.75**	**−5701.89**	584	513	[24]
	$Na_2Al_2Si_2O_8\cdot4.5H_2O$	**−20.5 ± 0.6**	**−5029.88**	**−5486.36**	536	475	[24]
Chabazite	$Ca_{3.2}K_{4.0}Na_{3.1}Al_{13.5}Si_{22.5}O_{72}\cdot36H_2O$		−43,622.6	−47,491.2	3974.3		[21]
	$Na_2Al_2Si_4O_{12}\cdot6H_2O$	**−31.9 ± 1.0**	**−7117.55**	**−7810.40**	552	578	[24]
	$CaAl_2Si_4O_{12}\cdot6H_2O$				640	589	[18]
	$CaAl_2Si_4O_{12}\cdot6H_2O$	**−25.80**	**−7111.8**	**−7774.0**	581	617	[8]
	$CaAl_2Si_4O_{12}\cdot6H_2O$	**−31.4 ± 0.9**	**−7144.01**	**−7806.74**	581	617	[10]
	$CaAl_2Si_4O_{12}\cdot6H_2O$	−34.22		−7824.4	614	643	[56]
Faujasite(X)	$Na_2Al_2Si_{2.5}O_9\cdot6.2H_2O$	**−20.10**	**−5847.5**	**−6447.0**	**566**	**586**	[8]
	$Na_2Al_2Si_{2.5}O_9\cdot6.2H_2O$	**−21.9 ± 0.7**	**−5857.79**	**−6456.94**	**566**	**586**	[24]
Faujasite(Y)	$Na_2Al_2Si_4O_{12}\cdot8H_2O$	**−25.00**	**−7552.5**	**−8327.0**	**734**	**739**	[8]
	$Na_2Al_2Si_4O_{12}\cdot8H_2O$	**−29.5 ± 0.9**	**−7578.22**	**−8352.62**	**734**	**739**	[24]
Natrolite	$Na_2Al_2Si_3O_{10}\cdot2H_2O$	−26.43	−5316.7	**−5718.6**	**360**	**359**	[59]
	$Na_2Al_2Si_3O_{10}\cdot H_2O$				**425**	**380**	[18]
	$Na_2Al_2Si_3O_{10}\cdot2H_2O$	**−30.20**	**−5325.7**	**−5728.0**	**360**	**359**	[8]
	$K_{1.86}Na_{0.01}Ca_{0.04}Mg_{0.01}Al_{1.96}Si_{3.04}O_{10}\cdot2.72H_2O$				**460.5 ± 0.6**	**433.3 ± 0.6**	[57]
Mordenite	$Ca_{0.25}K_{0.15}Na_{0.35}AlSi_5O_{12}\cdot3.667H_2O$		−6294.6	−6807.6			[14]
	$Na_{0.72}Al_{0.72}Si_{5.28}O_{12}\cdot2.71H_2O$	**−22.5 ± 0.7**	**−5954.97**	**−6442.54**	390	405	[24]
	$Ca_{0.289}Na_{0.361}Al_{0.940}Si_{5.060}O_{12}\cdot3.468H_2O$		−6229.89	−6738.44	486.54	484.45	[56]
	$Ca_{0.289}Na_{0.361}Al_{0.940}Si_{5.060}O_{12}\cdot3.468H_2O$	−30.68	**−6247.6 ± 4.5**	**−6756.2 ± 4.5**	**486.54 ± 0.97**	**484.33 ± 0.97**	[65]
	$Ca_{0.29}Na_{0.36}Al_{0.94}Si_{5.06}O_{12}\cdot3.47H_2O$		−6227.9	−6736.7	486.5		[18]
	$Ca_{0.34}Al_{0.68}Si_{5.33}O_{12}\cdot2.9H_2O$	**−21.6 ± 0.6**	**−6001.89**	**−6497.46**	386	404	[10]
	$Ca_{0.515}Al_{1.03}Si_{4.97}O_{12}\cdot3.10H_2O$	−26.48	−6165.4	−6662.2	470.6	443.1	[66]
	$Ca_{0.56}Al_{1.12}Si_{4.88}O_{12}\cdot3.90H_2O$	**−25.32 ± 0.13**	**−6275.0 ± 3.6**				[55]
Stilbite	$Ca_{1.019}Na_{0.136}K_{0.006}Al_{2.180}Si_{6.820}O_{18}\cdot7.33H_2O$	−55.22	**−10,142.0 ± 6.6**	**−11,033.6 ± 6.6**	**805.5 ± 1.6**	**808.7 ± 1.6**	[67]
	$CaNa_{0.5}Al_{2.5}Si_{6.5}O_{18}\cdot8H_2O$	−49.06	**−10,347.1**	**−11,289.9**	811	848	[68]
	$Ca_{1.01}Na_{0.12}Al_{2.12}Si_{6.88}O_{18}\cdot7.27H_2O$		**−10,130.9 ± 10.9**	**−11,017.9 ± 10.9**			[69]
	$Ca_{1.11}Al_{2.22}Si_{6.78}O_{18}\cdot6.8H_2O$	**−40.6 ± 1.2**	**−9960.24**	**−10,830.7**	**750**	800	[10]
Heulandite	$Ca_{0.86}Na_{0.37}K_{0.06}Al_{2.14}Si_{6.86}O_{18}\cdot6.1H_2O$	−55.06	**−9835.7 ± 8.6**	**−10,656.3 ± 8.6**	**765.0 ± 2.2**		[69]
	$Na_{0.365}K_{0.059}Ca_{0.861}Al_{2.138}Si_{6.860}O_{18}\cdot6.17H_2O$				**736 ± 8**	**752 ± 8**	[70]
	$Ba_{0.065}Sr_{0.175}Ca_{0.585}Na_{0.383}K_{0.132}Al_{2.165}Si_{6.835}O_{18}\cdot6H_2O$	−29.55	**−9675.7 ± 10.2**	**−10,491.0 ± 10.2**	**767.2 ± 0.8**	**781.0 ± 0.8**	[59]
	$Na_{2.14}Al_{2.14}Si_{6.86}O_{18}\cdot6.17H_2O$			−10,612.9	838	719	[56]
	$CaAl_2Si_7O_{18}\cdot6H_2O$	−45.02	**−9722.3 ± 6.3**	**−10,524.3 ± 9.6**	**783.7 ± 16**		[71]
	$Ca_{1.07}Al_{2.14}Si_{6.86}O_{18}\cdot6.17H_2O$			−10,667.2	701	719	[56]
	$Ca_{1.07}Al_{2.14}Si_{6.86}O_{18}\cdot4.4H_2O$	**−40.4 ± 1.2**	**−9352.74**	**−10,117.2**	541	611	[10]
	$Ca_{1.07}Al_{2.14}Si_{6.86}O_{18}\cdot4.5H_2O$	**−39.3 ± 1.2**	**−9372.03**	**−10,132.1**	581	619	[10]
Clinoptilolite	$K_{1.10}Al_{1.10}Si_{4.90}O_{12}\cdot2.70H_2O$	**−28.11**	**−6107.4**	**−6568.4**	**508**	454	[23]
	$Na_{0.56}K_{0.98}Ca_{1.50}Mg_{1.23}(Al_{6.7}Fe_{0.3})Si_{29}O_{72}\cdot22H_2O$				**2872.3 ± 9.0**	**2986.5**	[63]
	$Na_{1.10}Al_{1.10}Si_{4.90}O_{12}\cdot3.50H_2O$	**−26.47**	**−6267.9**	**−6782.4**	**503**	470	[23]
	$Ca_{0.56}Al_{1.12}Si_{4.88}O_{12}\cdot3.90H_2O$	−27.51		−6923.3	499	481	[56]
	$Ca_{0.52}Al_{1.04}Si_{4.97}O_{12}\cdot3.1H_2O$	**−23.6 ± 0.7**	**−6146.38**	**−6635.48**	**454**	449	[10]
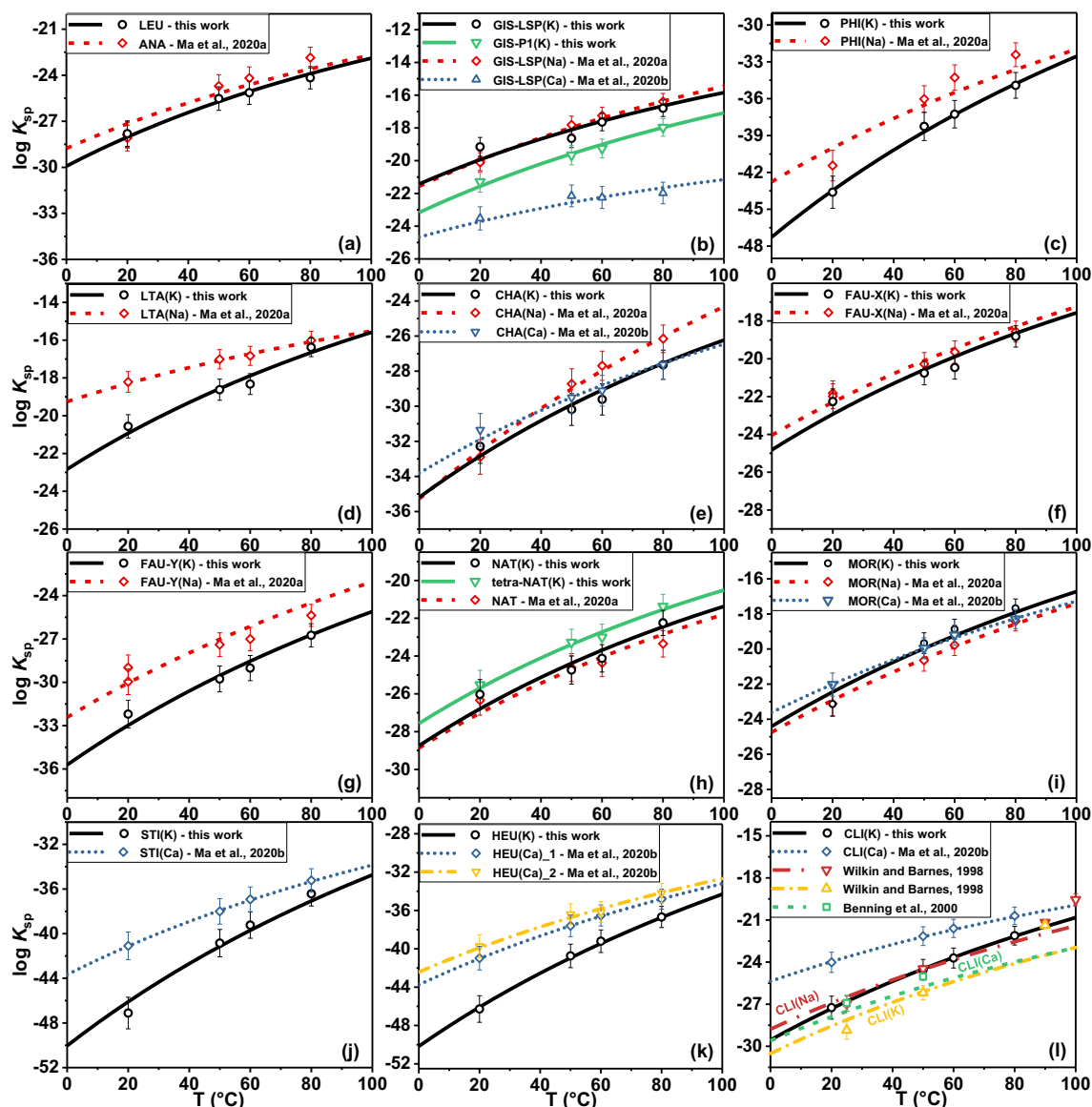
Fig. 4. The log K_{sp} values at different temperatures and the fit curve for (a) LEU, (b) GIS-LSP(K) and GIS-P1(K), (c) PHI(K), (d) LTA(K), (e) CHA(K), (f) FAU-X(K), (g) FAU-Y(K), (h) NAT(K) and tetra-NAT(K), (i) MOR(K), (j) STI(K), (k) HEU(K), and (l) CLI(K). For comparison, the solubility data of the corresponding Na- or Ca-endmembers as reported in Ma et al. [24] and Ma et al. [10] as well as the literature data of clinoptilolites [23,55] were also plotted.

25 °C based on the measured logK$_{sp}$ values at different temperatures for each zeolite, based on Eqs. (2) and (3). The C_p^0 value was estimated using the additivity method or derived from literature data was added to complete the thermodynamic data of each zeolite.

The produced standard thermodynamic data of K-based zeolites are shown in Table 5. The entropy S fitted based on the increase of solubility with temperature were in the same range as the C_p^0 value, indicating a reasonable consistency between these data. For comparison, literature data of the zeolites that have the same frameworks are reviewed and tabulated in Table 6. As shown in Table 6, the dominant cations of the reported zeolites are typically Na$^+$ and Ca^{2+}, rather than K$^+$. Only for leucite, K-phillipsite, and K-clinoptilolite data are available for K$^+$ as the major host cations. Fig. 4 shows the log K$_{sp}$ values and the curve fitted for each K-based zeolite and the comparison with the data of the corresponding Na- and/or Ca-endmember (from Table 6).

In a first step, the obtained data for K-based zeolites were compared with their Na-based counterparts, where similar trends were expected based on the similarities in charge and size between the two cations. In the temperature range of 0 to 100 °C, K-based zeolites typically have

lower solubility (more negative log K$_{sp}$ value) than the corresponding Na-based and Ca-based zeolites (Fig. 4), with the exception of the zeolites having GIS, NAT, and MOR frameworks. This indicates that many K-based zeolites are thermodynamically more stable than their Na- or Ca-endmembers. In most cases, the solubility of the K-based zeolites increases from 0 to 100 °C with a greater rate of change than those of Na- and Ca-endmembers, except for zeolites having GIS and CHA framework. This trend indicates that at temperatures ≫ 100 °C, in many cases the Ca and/or Na-endmembers can be expected to be more stable than their K-based analogues. This phenomenon can be verified for clinoptilolites based on the solubility measurements reported by Benning et al. [55] and Wilkin and Barnes [23]. At 25 °C, the log K$_{sp}$ values of the clinoptilolite varieties increased (Table 6) in an order of K-endmember (−28.11 for K$_{1.10}$Al$_{1.10}$Si$_{4.90}$O$_{12}$·2.70H$_2$O) < Ca-endmember (−27.51 for Ca$_{0.56}$Al$_{1.12}$Si$_{4.88}$O$_{12}$·3.90H$_2$O) < Na-endmember (−26.47 for Na$_{1.10}$Al$_{1.10}$Si$_{4.90}$O$_{12}$·3.50H$_2$O) [23,56]. In contrast, in the temperature range of 100 to 300 °C, the Ca-based clinoptilolite resulted in the lowest log K$_{sp}$ value, while the Na-endmember was the most soluble [55], confirming the trends observed here below 100 °C.
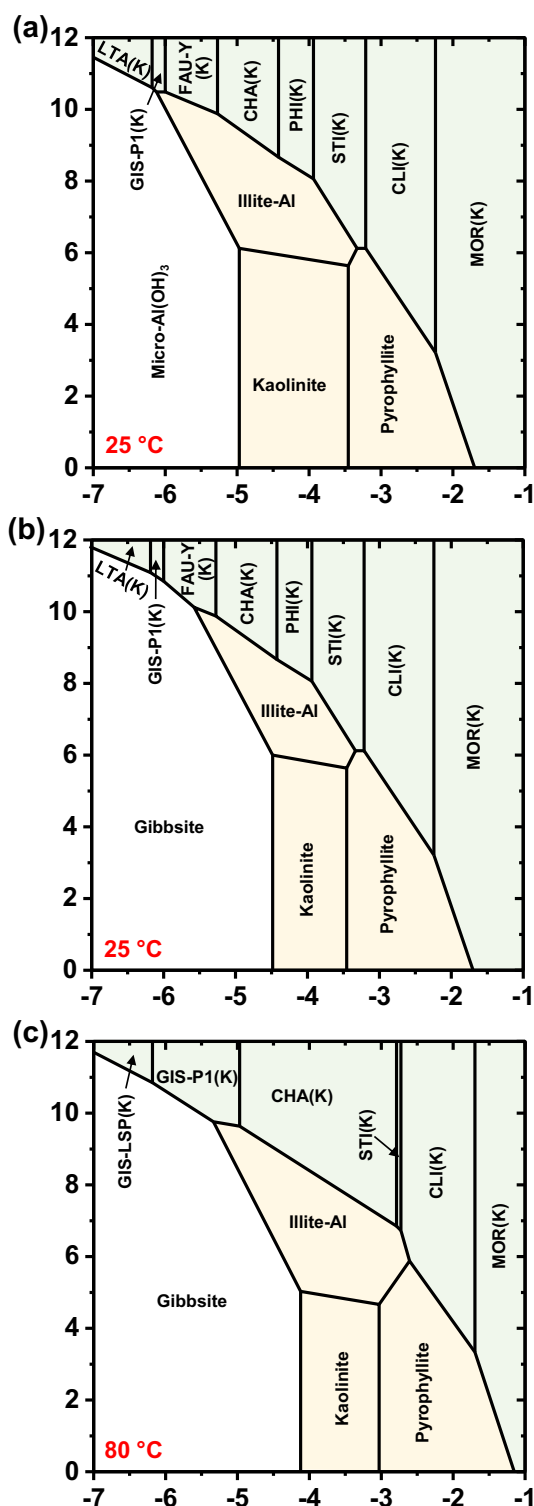
Fig. 5. Predominance diagrams in K_2O-SiO_2-Al_2O_3-H_2O chemical systems for zeolite (light green), clay and mica (light yellow), and $Al(OH)_3$ (colorless) phases. (a) System saturated with respect to microcrystalline $Al(OH)_3$ (micro-Al$(OH)_3$) at 25 °C; system saturated with respect to gibbsite (b) at 25 °C and (c) at 80 °C. (For interpretation of the references to colour in this figure legend, the reader is referred to the web version of this article.)

The exceptional cases observed from the trends are worth to be discussed further. Regarding GIS (Fig. 4b), GIS-LSP(K) shows a comparable solubility to GIS-LSP(Na) from 0 to 100 °C. In contrast, GIS-LSP(Ca) resulted in the most negative log K_{sp} value among the GIS-LSP

varieties and even more negative values at higher temperatures as expected from the fit curves. It indicates that GIS-LSP(Ca) is the most thermodynamically stable GIS zeolite, in good accordance with the gismondine observed in nature [27] and the experimental observations in literatures [8,56]. For K-based GIS, GIS-P1(K) (Si/Al ratio = 1.4) has a higher Si/Al ratio and shows a lower solubility compared with GIS-LSP (K) (Si/Al ratio = 1.0), suggesting that the Si/Al ratio strongly affects the solubility of zeolites as also discussed in [56]. Regarding CHA (Fig. 4e), CHA(K) is slightly more stable than CHA(Na) and CHA(Ca) between 20 and ~80 °C, whereas above the stability order changed to be CHA(Ca) > CHA(K) > CHA(Na). Regarding NAT (Fig. 4h), the solubility results indicated a good agreement with the predominance of natrolite among NAT zeolites in nature [27], rather than K-based natrolite. As characterized by XRD, tetra-NAT(K) has a disordered distribution of Si and Al T-sites in tetragonal symmetry while NAT(K) has ordered T-sites distribution in orthorhombic symmetry. The lower solubility of NAT(K) than tetra-NAT(K) as observed here might result from the more ordered T-sites distribution in NAT(K), or from the presence of the tiny amount of K-doped natrolite. The log K_{sp} values of the K-doped natrolite ($Na_{15.62}K_{0.46}Al_{16}Si_{24}O_{80}\cdot15.36H_2O$) were calculated using the aqueous results of NAT(K) dissolution experiments and shown in the footnote of Table 4, which indicates a slightly lower solubility than NAT [24]. Moreover, the generated S^0 (416 J/mol/K) and C_p^0 (370 J/mol/K) of NAT (K) agree well with the recalculated values (420 and 401 J/mol/K for S^0 and C_p^0, respectively, with the unified formula of $K_2Al_2Si_3O_{10}\cdot2H_2O$) based on the calorimetry data of a K-substituted natrolite ($K_{1.86}Na_{0.01}Ca_{0.04}Mg_{0.01}Al_{1.96}Si_{3.04}O_{10}\cdot2.72H_2O$) [57].

Regarding MOR (Fig. 4i), the solubility of the three varieties of cations was quite close although MOR(Na) was slightly more stable. With increasing temperature, the solubility of MOR(K) increases the most quickly while that of MOR(Ca) the most slowly.

3.3. Predominance diagrams in the chemical sub-systems of K_2O-SiO_2-Al_2O_3-H_2O

Predominance diagrams of solid phases in the chemical sub-systems of K_2O-SiO_2-Al_2O_3-H_2O at 25 and 80 °C were drawn, as shown in Figs. 5 and 6, in order to predict the formation of zeolites at cement/clay interfaces that are expected to be widespread in cement-rich nuclear waste repositories. The diagrams show a good consistency between the newly generated thermodynamic data of the K-based zeolites, the Cemdata18 database [25], and the data of clays/micas in the THERMOCHIMIE database [26]. Through employing the thermodynamic data of more types of K-based zeolites, a more refined predominance zone of zeolites could be plotted here, compared to the predominance diagrams presented by Blanc et al. [56].

Specifically, the chemical sub-systems saturated with microcrystalline $Al(OH)_3$ (micro-Al$(OH)_3$) at 25 °C and with gibbsite ($Al(OH)_3$) at both 25 and 80 °C were investigated. Micro-Al$(OH)_3$ is expected to be thermodynamically stable only at relatively low temperatures (e.g., 25 °C). As shown in Fig. 5a, under mild conditions of {K^+/H^+} and {SiO_2}, illite-Al, kaolinite, and pyrophyllite were predicted to predominate, in accordance with Blanc et al. [56]. Under chemical conditions of either high {K^+/H^+} or high {SiO_2}, the stability domains were occupied by various types of zeolites. With increasing {SiO_2}, the zeolites were predicted to be LTA(K), GIS-P1(K), FAU-Y(K), CHA(K), PHI(K), STI (K), CLI(K), and MOR(K) in sequence, with their corresponding Si/Al ratios increasing from 1.00, 1.40, 1.75, 2.00, 2.20, 3.09, 4.94, to 8.23. The consistent increase tendency between {SiO_2} and Si/Al ratio indicates a good internal consistency of the thermodynamic data of K-based zeolites. Compared to micro-Al$(OH)_3$ at 25 °C the predominance area of gibbsite (Fig. 5b) obviously expands and thus compresses the domains of neighbor phases (i.e., LTA(K), GIS-P1(K), FAU-Y(K), illite-Al, and kaolinite), which is the only distinction between the cases of gibbsite and micro-Al$(OH)_3$ at 25 °C. At 80 °C, the stability domain of gibbsite expands more and the domains of zeolites are predominated in
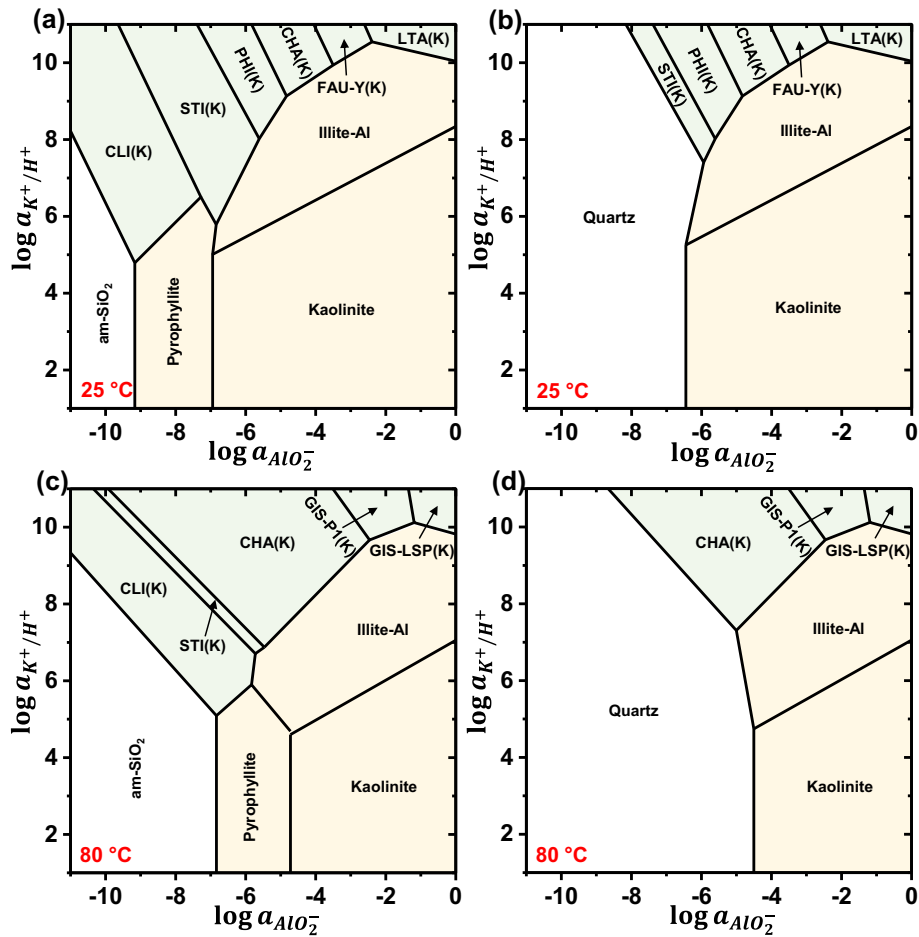
Fig. 6. Predominance diagrams in K_2O-SiO_2-Al_2O_3-H_2O chemical systems for zeolite (light green), clay and mica (light yellow), and SiO_2 (colorless) phases. System saturated with respect to (a) amorphous SiO_2 (am-SiO_2) or (b) quartz at 25 °C; system saturated with respect to (c) am-SiO_2 or (d) quartz at 80 °C. (For interpretation of the references to color in this figure legend, the reader is referred to the web version of this article.)

sequence by GIS-LSP(K), GIS-P1(K), CHA(K), STI(K), CLI(K), and MOR (K) with increasing {SiO_2}. It suggests that these six zeolites are favored at high temperatures.

Regarding the chemical sub-systems saturated with respect to SiO_2, amorphous SiO_2 (am-SiO_2) can provide much higher concentrations of Si than quartz, a highly crystalline form of SiO_2. In the saturated system of am-SiO_2 (Fig. 6a and c), CLI(K) and pyrophyllite, the minerals with relatively higher Si/Al ratios compared to kaolinite, illite-Al, and other zeolites, are able to form both at 25 °C and at 80 °C. With increasing {AlO_2^-} at 25 °C, the predominated zeolites are predicted to be CLI(K), STI(K), PHI(K), CHA(K), FAU-Y(K), and LTA(K) in sequence, agreeing well with their decreasing Si/Al ratios. In contrast, no CLI(K) and py-rophyllite were predicted to exist in the systems saturated with quartz at both 25 and 80 °C (Fig. 6b and d), indicating that the Si concentration controlled by the saturation of quartz is not high enough to support the formation of high-silica zeolites (like MOR(K) and CLI(K)). With increasing temperature, the stability domain of quartz expands; three types of K-based zeolites, i.e., CHA(K), GIS-P1(K), and GIS-LSP(K), are predicted to be more thermodynamically stable.

In comparison to our previous study on Na-based zeolites where Na-based phillipsite was predicted to be unstable in the cement/clay interaction system [24], the predominance diagrams here illustrate that the K-based phillipsite (PHI(K)) is favored to form under suitable ranges of {K^+/H^+}, {SiO_2}, and {AlO_2^-}. Note that K^+ is found to be the major extraframework cation of the most common phillipsite in nature [27]. Based on adequate experimental observations, Gaucher and Blanc elaborated that K-rich phillipsite could commonly form in cement/clay

interaction systems [11]. In fact the formation of K-dominated phil-lipsite was observed at a cement clay interface at 70 °C after 1 year [12], which validates our current results with PHI(K). Typically, phillipsite tends to accommodate also some Na^+ or Ca^{2+} as minor cations to form solid solutions of K^+-Na^+ or K^+-Ca^{2+}. Such solid solution are expected to be more thermodynamically stable than their Na- or Ca-endmembers in the presence of potassium. Further studies will focus on the effect of solid solutions on zeolite solubility.

Note that an exact agreement between the currently developed predominance diagrams and the natural abundance or previous mineral observations might not be always reached as the stability domains are only predicted based on the oversaturation degree of limited types of K-based zeolites.

4. Conclusions

In this study, 14 types of K-based zeolites, based on six different secondary building units (i.e., S4R, D4R, D6R, 4 = 1, 5-1, and 4-4 = 1), were synthesized by hydrothermal K^+-exchange methods based on their corresponding Na- and Ca-based endmembers resulting in K-based ze-olites of high purity. Based on the combination of XRD, FT-IR, SEM-EDS, and TGA data the framework structure (i.e., ANA, GIS, PHI, LTA, CHA, FAU, NAT, MOR, STI, or HEU) and the elemental composition of each zeolite were determined.

The solubility products (K_{sp}) of the zeolites were determined experimentally at 20, 50, 60, and 80 °C from under-saturation and compared with published values of their Na- and/or Ca-endmembers.

The K-based zeolites typically showed the lowest solubility in the temperature range 0 to 100 °C, with the notable exception of zeolites having GIS, NAT, and MOR frameworks.

The solubility of the investigated K-based zeolite increased strongly with temperature, in most cases more than those of Na- or Ca-based zeolites, indicating that at lower temperature K-based zeolites can be expected to form while higher temperature Na and Ca-based zeolites can be expected. This temperature tendency agrees well with the few solubility data reported in literatures, where for K-based clinoptilolite was reported to be most stable at 25 °C, while Ca-based clinoptilolite was stabilized between 100 and 300 °C [23,55].

Based on the measured solubility data at different temperatures, $\Delta_f G^0$, $\Delta_f H^0$, and S^0 of the zeolites were derived using GEM-Selektor; the heat capacity C_p^0 was obtained from reported experimental data or calculated by the additivity method. These thermodynamic data were used to establish predominance diagrams in the chemical sub-systems of K_2O-SiO_2-Al_2O_3-H_2O and compared with previous reports [56], which validated the good compatibility between the zeolite data, the selected K-based clays and micas from THERMOCHIMIE database, and the Cemdata18 database. LTA(K), GIS-LSP(K), GIS-P1(K), FAU-Y(K), CHA (K), PHI(K), STI(K), CLI(K), and MOR(K) were predicted to form possibly in such K-rich chemical systems relevant to cements, clays, and rock-forming minerals. This study provides crucial data to assess the formation process and the stability domain of K-based zeolites not only in the context of cement/clay-rich nuclear waste repositories but also in any environment where zeolites could exist (such as cement hydration and degradation processes).

This database for K-containing zeolites is together with the data for Na and Ca-zeolites freely downloadable at http://www.empa.ch/c emdata in formats supporting the computer programs GEM-Selektor [37,72] and in PHREEQC format.

CRediT authorship contribution statement

Bin Ma: Methodology, Investigation, Data curation, Formal analysis, Writing – original draft. **Barbara Lothenbach:** Conceptualization, Supervision, Resources, Writing – review & editing.

Declaration of competing interest

The authors declare that they have no known competing financial interests or personal relationships that could have appeared to influence the work reported in this paper.

Acknowledgements

Appendix A. Supplementary data

Supplementary data to this article can be found online at https://doi. org/10.1016/j.cemconres.2021.106537.

References

[1] B. Ahmadi, M. Shekarchi, Use of natural zeolite as a supplementary cementitious material, Cem. Concr. Compos. 32 (2010) 134–141.

[2] C. Shi, A. Fernández-Jiménez, Stabilization/solidification of hazardous and radioactive wastes with alkali-activated cements, J. Hazard. Mater. 137 (2006) 1656–1663.

[3] J.L. Provis, G.C. Lukey, J.S.J. van Deventer, Do geopolymers actually contain nanocrystalline zeolites? A reexamination of existing results, Chem. Mater. 17 (2005) 3075–3085.

[4] L. Wang, D.A. Geddes, B. Walkley, J.L. Provis, V. Mechtcherine, D.C. Tsang, The role of zinc in metakaolin-based geopolymers, Cem. Concr. Res. 136 (2020) 106194.

[5] M.D. Jackson, S.R. Mulcahy, H. Chen, Y. Li, Q. Li, P. Cappelletti, H.-R. Wenk, Phillipsite and Al-tobermorite mineral cements produced through low-temperature water-rock reactions in Roman marine concrete, Am. Mineral. 102 (2017) 1435–1450.

[6] Z. Shi, C. Shi, J. Zhang, S. Wan, Z. Zhang, Z. Ou, Alkali-silica reaction in waterglass-activated slag mortars incorporating fly ash and metakaolin, Cem. Concr. Res. 108 (2018) 10–19.

[7] Z. Shi, B. Ma, B. Lothenbach, Effect of Al on the formation and structure of alkali-silica reaction products, Cem. Concr. Res. 140 (2021) 106311.

[8] B. Lothenbach, E. Bernard, U. Mäder, Zeolite formation in the presence of cement hydrates and albite, Phys. Chem. Earth. Pt. A/B/C 99 (2017) 77–94.

[9] R. Fernández, M. Rodríguez, R.V.D.L. Villa, J. Cuevas, Geochemical constraints on the stability of zeolites and C–S–H in the high pH reaction of bentonite, Geochim. Cosmochim. Acta 74 (2010) 890–906.

[10] B. Ma, B. Lothenbach, Thermodynamic study of cement/rock interactions using experimentally generated solubility data of zeolites, Cem. Concr. Res. 135 (2020) 106149.

[11] E.C. Gaucher, P. Blanc, Cement/clay interactions — a review: experiments, natural analogues, and modeling, Waste Manag. 26 (2006) 776–788.

[12] P. Lalan, A. Dauzères, L. De Windt, D. Bartier, J. Sammaljärvi, J.-D. Barnichon, I. Techer, V. Detilleux, Impact of a 70 °C temperature on an ordinary Portland cement paste/claystone interface: an in situ experiment, Cem. Concr. Res. 83 (2016) 164–178.

[13] I. Petrovic, A. Navrotsky, Thermochemistry of Na-faujasites with varying Si/Al ratios, Micropor. Mater. 9 (1997) 1–12.

[14] R. Arthur, H. Sasamoto, C. Walker, M. Yui, Polymer model of zeolite thermochemical stability, Clay Clay Miner. 59 (2011) 626–639.

[15] S.V. Mattigod, B.P. McGrail, Estimating the standard free energy of formation of zeolites using the polymer model, Microporous Mesoporous Mater. 27 (1999) 41–47.

[16] R.J. Myers, B. Lothenbach, S.A. Bernal, J.L. Provis, Thermodynamic modelling of alkali-activated slag cements, Appl. Geochem. 61 (2015) 233–247.

[17] G.M. Anderson, D.A. Crerar, Thermodynamics in Geochemistry: The Equilibrium Model, Oxford University Press, 1993.

[18] H.C. Helgeson, J.M. Delany, H.W. Nesbitt, D.K. Bird, Summary and critique of the thermodynamic properties of rock-forming minerals, Am. J. Sci. 278 (1978) 1–229.

[19] A. La Iglesia, A.J. Aznar, A method of estimating the Gibbs energies of formation of zeolites, Zeolites 6 (1986) 26–29.

[20] J.A. Chermak, J.D. Rimstidt, Estimating the thermodynamic properties (ΔG°_f and ΔH°_f) of silicate minerals at 298 K from the sum of polyhedral contributions, Am. Mineral. 74 (1989) 1023–1031.

[21] S.J. Chipera, J.A. Apps, Geochemical stability of natural zeolites, Rev. Mineral. Geochem. 45 (2001) 117–161.

[22] T.S. Bowers, R.G. Burns, Activity diagrams for clinoptilolite; susceptibility of this zeolite to further diagenetic reactions, Am. Mineral. 75 (1990) 601–619.

[23] R.T. Wilkin, H.L. Barnes, Solubility and stability of zeolites in aqueous solution; I, analcime, Na-, and K-clinoptilolite, Am. Mineral. 83 (1998) 746–761.

[24] B. Ma, B. Lothenbach, Synthesis, characterization, and thermodynamic study of selected Na-based zeolites, Cem. Concr. Res. 135 (2020) 106111.

[25] B. Lothenbach, D.A. Kulik, T. Matschei, M. Balonis, L. Baquerizo, B. Dilnesa, G. D. Miron, R.J. Myers, Cemdata18: a chemical thermodynamic database for hydrated Portland cements and alkali-activated materials, Cem. Concr. Res. 115 (2019) 472–506.

[26] E. Giffaut, M. Grivé, P. Blanc, P. Vieillard, E. Colàs, H. Gailhanou, S. Gaboreau, N. Marty, B. Made, L. Duro, Andra thermodynamic database for performance assessment: ThermoChimie, Appl. Geochem. 49 (2014) 225–236.

[27] G. Glauco, G. Ermanno, Natural Zeolites, Springer, 1985.

[28] A. Vollpracht, B. Lothenbach, R. Snellings, J. Haufe, The pore solution of blended cements: a review, Mater. Struct. 49 (2016) 3341–3367.

[29] X. Ke, S.A. Bernal, T. Sato, J.L. Provis, Alkali aluminosilicate geopolymers as binders to encapsulate strontium-selective titanate ion-exchangers, Dalton Trans. 48 (2019) 12116–12126.

[30] N. Soonthornwiphat, Y. Kobayashi, K. Toda, K. Kuroda, C.R. Islam, T. Otake, Y. Elakneswaran, J.L. Provis, T. Sato, Encapsulation of Sr-loaded titanate spent adsorbents in potassium aluminosilicate geopolymer, J. Nucl. Sci. Technol. 57 (2020) 1181–1188.

[31] P. Lalan, A. Dauzères, L. De Windt, J. Sammaljärvi, D. Bartier, I. Techer, V. Detilleux, M. Siitari-Kauppi, Mineralogical and microstructural evolution of Portland cement paste/argillite interfaces at 70 °C — considerations for diffusion and porosity properties, Cem. Concr. Res. 115 (2019) 414–425.

[32] B.Y. Zhen-Wu, D.P. Prentice, J.V. Ryan, K. Ellison, M. Bauchy, G. Sant, zeo19: a thermodynamic database for assessing zeolite stability during the corrosion of nuclear waste immobilization glasses, npj Mater. Degrad. 4 (2020) 2.

[33] B. Ma, B. Lothenbach, Influences of Tetrahedral Atom Ordering and Si/Al Ratio on Thermodynamic Properties of Selected Zeolites, 2021 (In preparation).

[34] J. Shin, N.H. Ahn, M.A. Camblor, C.M. Zicovich-Wilson, S.B. Hong, Synthesis of aluminosilicate natrolites and control of their tetrahedral atom ordering, Chem. Mater. 26 (2014) 3361–3363.

[35] B.R. Albert, A.K. Cheetham, J.A. Stuart, C.J. Adams, Investigations on P zeolites: synthesis, characterisation, and structure of highly crystalline low-silica NaP, Microporous Mesoporous Mater. 21 (1998) 133–142.

[36] P. Sharma, J.-S. Song, M.H. Han, C.-H. Cho, GIS-NaP1 zeolite microspheres as potential water adsorption material: influence of initial silica concentration on adsorptive and physical/topological properties, Sci. Rep. 6 (2016) 22734.

[37] D.A. Kulik, T. Wagner, S.V. Dmytrieva, G. Kosakowski, F.F. Hingerl, K. V. Chudnenko, U.R. Berner, GEM-Selektor geochemical modeling package: revised algorithm and GEMS3K numerical kernel for coupled simulation codes, Comput. Geosci. 17 (2013) 1–24.

[38] B.J. Merkel, B. Planer-Friedrich, Groundwater Geochemistry: A Practical Guide to Modeling of Natural and Contaminated Aquatic Systems, Springer, Berlin, 2008.

[39] R.G. Berman, Internally-consistent thermodynamic data for minerals in the system $Na_2O-K_2O-CaO-MgO-FeO-Fe_2O_3-Al_2O_3-SiO_2-TiO_2-H_2O-CO_2$, J. Petrol. 29 (1988) 445–522.

[40] D.A. Kulik, Minimising Uncertainty Induced by Temperature Extrapolations of Thermodynamic Data: A Pragmatic View on the Integration of Thermodynamic Databases into Geochemical Computer Codes, Nuclear Energy Agency of the OECD (NEA), 2002.

[41] R.A. Robie, B.S. Hemingway, Thermodynamic Properties of Minerals and Related Substances at 298.15 K and 1 bar (10^5 Pascals) Pressure and at Higher Temperatures Vol. 2131, US Government Printing Office, 1995.

[42] M.W.J. Chase, NIST-JANAF Thermochemical Tables: National Institute of Standards and Technology, in: J Phys Chem Ref Data, Fourth edition, vol. 9, 1998.

[43] T. Thoenen, W. Hummel, U. Berner, E. Curti, The PSI/Nagra chemical thermodynamic database 12/07, in: Nagra Working Report NAB, 2014.

[44] D.L. Parkhurst, C. Appelo, Description of input and examples for PHREEQC version 3: a computer program for speciation, batch-reaction, one-dimensional transport, and inverse geochemical calculations, in: US Geological Survey, 2013.

[45] D. Kinniburgh, D. Cooper, PhreePlot: Creating Graphical Output With PHREEQC, 2011.

[46] A. Kloužková, M. Mrázová, M. Kohoutková, Synthesis of partially stabilized leucite, J. Phys. Chem. Solids 68 (2007) 1207–1210.

[47] J.N. Israelachvili, 4 - interactions involving polar molecules, in: J.N. Israelachvili (Ed.), Intermolecular and Surface Forces, Third edition, Academic Press, San Diego, 2011, pp. 71–90.

[48] B. Lothenbach, P. Durdziński, K.D. Weerdt, Thermogravimetric analysis, in: K. Scrivener, R. Snellings, B. Lothenbach (Eds.), A Practical Guide to Microstructural Analysis of Cementitious Materials, Taylor & Francis Group, 2016, pp. 177–212.

[49] M. Földvári, Handbook of the Thermogravimetric System of Minerals and Its Use in Geological Practice, Occasional Papers of the Geological Institute of Hungary, Budapest, 2013.

[50] E.M. Flanigen, H. Khatami, H.A. Szymanski, Infrared structural studies of zeolite frameworks, in: E.M. Flanigen, L.B. Sand (Eds.), Molecular Sieve Zeolites-I, Advances in Chemistry, American Chemical Society, 1974, pp. 201–229.

[51] W. Mozgawa, M. Krol, K. Barczyk, FT-IR studies of zeolites from different structural groups, Chemik 65 (2011) 667–674.

[52] J. Scherzer, J.L. Bass, Infrared spectra of ultrastable zeolites derived from type Y zeolites, J. Catal. 28 (1973) 101–115.

[53] P.D. Glynn, E.J. Reardon, Solid-solution aqueous-solution equilibria; thermodynamic theory and representation, Am. J. Sci. 290 (1990) 164–201.

[54] S.M. Leisinger, B. Lothenbach, G. Le Saout, C.A. Johnson, Thermodynamic modeling of solid solutions between monosulfate and monochromate $3CaO·Al_2O_3·Ca[(CrO_4)_x(SO_4)_{1−x}]·nH_2O$, Cem. Concr. Res. 42 (2012) 158–165.

[55] L.G. Benning, R.T. Wilkin, H.L. Barnes, Solubility and stability of zeolites in aqueous solution: II. Calcic clinoptilolite and mordenite, Am. Miner. 85 (2000) 495–508.

[56] P. Blanc, P. Vieillard, H. Gailhanou, S. Gaboreau, N. Marty, F. Claret, B. Madé, E. Giffaut, ThermoChimie database developments in the framework of cement/clay interactions, Appl. Geochem. 55 (2015) 95–107.

[57] I.E. Paukov, J.A. Kowalewskoja, J.W. Seretkin, I.A. Belitzkij, Thermodynamic properties and structure of potassium-substituted natrolite in the phase transition region, Russ. J. Phys. Chem. A 76 (2002) 1560–1564.

[58] I.E. Paukov, I.A. Belitsky, B.A. Fursenko, Heat capacity and thermodynamic functions of leucite at low temperatures, Thermochim. Acta 387 (2002) 23–28.

[59] G. Johnson, H. Flotow, P. O'Hare, W. Wise, Thermodynamic studies of zeolites; natrolite, mesolite and scolecite, Am. Mineral. 68 (1983) 1134–1145.

[60] P.S. Neuhoff, G.L. Hovis, G. Balassone, J.F. Stebbins, Thermodynamic properties of analcime solid solutions, Am. J. Sci. 304 (2004) 21–66.

[61] W.M. Murphy, R.T. Pabalan, J.D. Prikryl, C.J. Goulet, Reaction kinetics and thermodynamics of aqueous dissolution and growth of analcime and Na-clinoptilolite at 25 °C, Am. J. Sci. 296 (1996) 128–186.

[62] E.G. King, Low temperature heat capacity and entropy at 298.16 K of analcite, J. Am. Chem. Soc. 77 (1955) 2192–2193.

[63] B.S. Hemingway, R.A. Robie, Thermodynamic properties of zeolites: low-temperature heat capacities and thermodynamic functions for phillipsite and clinoptilolite. Estimates of the thermochemical properties of zeolitic water at low temperature, Am. Miner. 69 (1984) 692–700.

[64] L. Qiu, V. Murashov, M.A. White, Zeolite 4A: heat capacity and thermodynamic properties, Solid State Sci. 2 (2000) 841–846.

[65] G. Johnson, I. Tasker, H. Flotow, P. O'Hare, W. Wise, Thermodynamic studies of mordenite, dehydrated mordenite, and gibbsite, Am. Mineral. 77 (1992) 85–93.

[66] P. Blanc, P. Vieillard, H. Gailhanou, S. Gaboreau, E. Gaucher, C.I. Fialips, B. Madé, E. Giffaut, A generalized model for predicting the thermodynamic properties of clay minerals, Am. J. Sci. 315 (2015) 734–780.

[67] D.A. Howell, G.K. Johnson, I.R. Tasker, P.A.G. O'Hare, W.S. Wise, Thermodynamic properties of the zeolite stilbite, Zeolites 10 (1990) 525–531.

[68] T. Fridriksson, P.S. Neuhoff, S. Arnórsson, D.K. Bird, Geological constraints on the thermodynamic properties of the stilbite—stellerite solid solution in low-grade metabasalts, Geochim. Cosmochim. Acta 65 (2001) 3993–4008.

[69] I. Kiseleva, A. Navrotsky, I. Belitsky, B. Fursenko, Thermochemical study of calcium zeolites–heulandite and stilbite, Am. Miner. 2001, 448 pp.

[70] V. Drebushchak, V. Naumov, V. Nogteva, I. Belitsky, I. Paukov, Low-temperature heat capacity of heulandite: comparison with clinoptilolite, Thermochim. Acta 348 (2000) 33–40.

[71] M. Cho, S. Maruyama, J.G. Liou, An experimental investigation of heulandite-laumontite equilibrium at 1000 to 2000 bar Pfluid, Contrib. Mineral. Petrol. 97 (1987) 43–50.

[72] T. Wagner, D.A. Kulik, F.F. Hingerl, S.V. Dmytrieva, GEM-Selektor geochemical modeling package: TSolMod library and data interface for multicomponent phase models, Can. Mineral. 50 (2012) 1173–1195.